The Astrophysical Journal, 898:161 (19pp), 2020 August 1 https://doi.org/10.3847/1538-4357/ab9f3d

The Rise and Fall of ASASSN-18pg: Following a TDE from Early to Late Times

Thomas W.-S. Holoien[1,21], Katie Auchettl[2,3,4,5], Michael A. Tucker[6,22], Benjamin J. Shappee[6], Shannon G. Patel[1], James C. A. Miller-Jones[7], Brenna Mockler[5], Danièl N. Groenewald[8,9], Jason T. Hinkle[6], Jonathan S. Brown[5], Christopher S. Kochanek[10,11], K. Z. Stanek[10,11], Ping Chen[12], Subo Dong[12], Jose L. Prieto[13,14], Todd A. Thompson[10,11], Rachael L. Beaton[1,15,23,24], Thomas Connor[1], Philip S. Cowperthwaite[1,25], Linnea Dahmen[16], K. Decker French[1,25], Nidia Morrell[17], David A. H. Buckley[8], Mariusz Gromadzki[18], Rupak Roy[19], David A. Coulter[5], Georgios Dimitriadis[5], Ryan J. Foley[5], Charles D. Kilpatrick[5], Anthony L. Piro[1], César Rojas-Bravo[5], Matthew R. Siebert[5], and Sjoert van Velzen[20]

[1] The Observatories of the Carnegie Institution for Science, 813 Santa Barbara St., Pasadena, CA 91101, USA; tholoien@carnegiescience.edu
[2] DARK, Niels Bohr Institute, University of Copenhagen, Lyngbyvej 2, DK-2100 Copenhagen, Denmark
[3] School of Physics, The University of Melbourne, Parkville, VIC 3010, Australia
[4] ARC Centre of Excellence for All Sky Astrophysics in 3 Dimensions (ASTRO 3D), Australia
[5] Department of Astronomy and Astrophysics, University of California, Santa Cruz, CA 95064, USA
[6] Institute for Astronomy, University of Hawai'i, 2680 Woodlawn Drive, Honolulu, HI 96822, USA
[7] International Centre for Radio Astronomy Research—Curtin University, GPO Box U1987, Perth, WA 6845, Australia
[8] South African Astronomical Observatory, P.O. Box 9, Observatory 7935, Cape Town, South Africa
[9] Southern African Large Telescope Foundation, P.O. Box 9, Observatory 7935, South Africa
[10] Center for Cosmology and AstroParticle Physics (CCAPP), The Ohio State University, 191 W. Woodruff Ave., Columbus, OH 43210, USA
[11] Department of Astronomy, The Ohio State University, 140 West 18th Avenue, Columbus, OH 43210, USA
[12] Kavli Institute for Astronomy and Astrophysics, Peking University, Yi He Yuan Road 5, Hai Dian District, Beijing 100871, People's Republic of China
[13] Núcleo de Astronomía de la Facultad de Ingeniería y Ciencias, Universidad Diego Portales, Av. Ejército 441, Santiago, Chile
[14] Millennium Institute of Astrophysics, Santiago, Chile
[15] Department of Astrophysical Sciences, Princeton University, 4 Ivy Lane, Princeton, NJ 08544, USA
[16] Department of Physics & Astronomy, Pomona College, 610 N College Ave, Claremont, CA 91711, USA
[17] Las Campanas Observatory, Carnegie Observatories, Casilla 601, La Serena, Chile
[18] Astronomical Observatory, University of Warsaw, Al. Ujazdowskie 4, 00-478 Warszawa, Poland
[19] The Inter-University Centre for Astronomy and Astrophysics, Ganeshkhind, Pune—411007, India
[20] Center for Cosmology and Particle Physics, New York University, NY 10003, USA
Received 2020 March 27; revised 2020 June 16; accepted 2020 June 19; published 2020 August 4

Abstract

We present nearly 500 days of observations of the tidal disruption event (TDE) ASASSN-18pg, spanning from 54 days before peak light to 441 days after peak light. Our data set includes X-ray, UV, and optical photometry, optical spectroscopy, radio observations, and the first published spectropolarimetric observations of a TDE. ASASSN-18pg was discovered on 2018 July 11 by the All-Sky Automated Survey for Supernovae (ASAS-SN) at a distance of $d = 78.6$ Mpc; with a peak UV magnitude of $m \simeq 14$, it is both one of the nearest and brightest TDEs discovered to-date. The photometric data allow us to track both the rise to peak and the long-term evolution of the TDE. ASASSN-18pg peaked at a luminosity of $L \simeq 2.4 \times 10^{44}$ erg s^{-1}, and its late-time evolution is shallower than a flux $\propto t^{-5/3}$ power-law model, similar to what has been seen in other TDEs. ASASSN-18pg exhibited Balmer lines and spectroscopic features consistent with Bowen fluorescence prior to peak, which remained detectable for roughly 225 days after peak. Analysis of the two-component Hα profile indicates that, if they are the result of reprocessing of emission from the accretion disk, the different spectroscopic lines may be coming from regions between ∼10 and ∼60 lt-days from the black hole. No X-ray emission is detected from the TDE, and there is no evidence of a jet or strong outflow detected in the radio. Our spectropolarimetric observations indicate that the projected emission region is likely not significantly aspherical, with the projected emission region having an axis ratio of $\gtrsim$0.65.

Unified Astronomy Thesaurus concepts: Black holes (162); Accretion (14); Galaxy accretion disks (562); Black hole physics (159); Supermassive black holes (1663); Tidal disruption (1696)

Supporting material: data behind figure, machine-readable table

1. Introduction

When a star passes too close to a supermassive black hole (SMBH) and crosses its tidal radius, the tidal shear forces from the SMBH overwhelm the self-gravity of the star, resulting in a tidal disruption event (TDE). For a main-sequence star, roughly half of the stellar material remains bound to the SMBH, initially falling back to pericenter at a rate proportional to $\sim t^{-5/3}$. A fraction of this material is accreted onto the SMBH, resulting in a luminous, short-lived flare (e.g., Lacy et al. 1982; Rees 1988; Evans & Kochanek 1989; Phinney 1989).

Initial theoretical work predicted that the emission from the TDE flare would peak at soft X-ray energies and that the luminosity would evolve at a rate proportional to the $t^{-5/3}$ mass fallback rate. Recent studies of TDEs, however, have revealed that TDEs exhibit a wide range of observational properties (e.g., van Velzen et al. 2011, 2019, 2020; Cenko et al. 2012;

[21] Carnegie Fellow.
[22] DOE Computational Science Graduate Fellow.
[23] Hubble Fellow.
[24] Carnegie-Princeton Fellow.
[25] Hubble Fellow.

Gezari et al. 2012, 2015, 2017; Arcavi et al. 2014; Chornock et al. 2014; Holoien et al. 2014, 2016a, 2016b, 2018, 2019a, 2019b; Vinkó et al. 2015; Brown et al. 2016, 2017, 2018; Auchettl et al. 2017; Blagorodnova et al. 2017; Leloudas et al. 2019). We now know that the initial theoretical picture of TDE emission was too simplistic, as the emission depends on many factors, ranging from the disrupted star's physical properties (e.g., MacLeod et al. 2012; Kochanek 2016), the way the accretion stream evolves after disruption (e.g., Kochanek 1994; Strubbe & Quataert 2009; Guillochon & Ramirez-Ruiz 2013; Hayasaki et al. 2013, 2016; Piran et al. 2015; Shiokawa et al. 2015), radiative transfer effects (e.g., Gaskell & Rojas Lobos 2014; Strubbe & Murray 2015; Roth et al. 2016; Roth & Kasen 2018), and viewing angle (e.g., Dai et al. 2018). Despite the increasing number of known TDE flares, few have been observed in sufficient detail to differentiate between various theoretical predictions. In particular, very few TDEs have been discovered prior to peak light, making it difficult to study the early evolution of the stellar debris and the formation of the accretion disk.

Here, we present the discovery and follow-up observations of ASASSN-18pg, a TDE flare discovered by the All-Sky Automated Survey for Supernovae (ASAS-SN; Shappee et al. 2014) on 2018 July 11 in the galaxy WKK 6047. We announced the discovery of the transient on 2018 July 15 on the Transient Name Server, where it was given the designation AT 2018dyb,[26] noting that the ASAS-SN position of the transient was consistent with the nucleus of the presumed host galaxy. We obtained an optical spectrum on 2018 July 17 (Pan et al. 2018) and found that the transient exhibited a strong blue continuum and several broad emission features, notably hydrogen Balmer and helium I and II lines, which are features consistent with a TDE (e.g., Arcavi et al. 2014).

After classifying ASASSN-18pg as a possible TDE, we requested and were awarded target-of-opportunity (TOO) observations from the Neil Gehrels Swift Gamma-ray Burst Mission (Swift; Gehrels et al. 2004) UltraViolet and Optical Telescope (UVOT; Roming et al. 2005) and X-ray Telescope (XRT; Burrows et al. 2005) (Target ID: 10764). The Swift observations confirmed that the transient was UV-bright, but we did not detect any X-ray emission. Based on the spectra and UV-brightness of the source, we began an extended multi-wavelength campaign to monitor and characterize the emission of ASASSN-18pg. Due to the early detection and prompt announcement of discovery by the ASAS-SN team, we were able to begin follow-up data collection from Swift and various ground-based observatories well before the peak of the TDE's light curve, providing us with a rising light curve spanning from the *i* band to the Swift UV filters and beginning 41 days prior to peak light. ASASSN-18pg thus provides us with one of the best opportunities to study the early emission from a TDE. We note that, while early observations of ASASSN-18pg were the subject of a study by Leloudas et al. (2019), their study was primarily focused on spectroscopic evolution of the TDE, while our data set contains considerably more photometric data, and our treatment of the host galaxy (see Section 2.1) provides for more robust host flux removal, allowing us to perform more extensive analyses. We also present spectropolarimetric observations of ASASSN-18pg obtained with the Southern African Large Telescope (SALT; Buckley et al. 2006), the first such observations of a TDE.

In Section 2, we describe the predisruption data available for WKK 6047 and fit its physical properties. We also discuss our follow-up observations of the transient and the available prediscovery data available from ASAS-SN. In Section 3, we analyze the photometric data, fit the light curves with a TDE emission model, model the blackbody evolution of ASASSN-18pg, and compare it to other TDEs. In Section 4, we analyze the evolution of spectroscopic emission lines in ASASSN-18pg and discuss the results of spectropolarimetric observations of the transient taken near peak light. Finally, in Section 5, we summarize our findings and discuss the implications for future TDE studies.

2. Observations

2.1. Archival Data and Host Fits

Due to its southern decl., WKK 6047 was not previously observed by optical surveys such as the Sloan Digital Sky Survey (SDSS) or Pan-STARRS. However, we were able to retrieve archival observations of the host in the *gri* filters obtained with DECam mounted on the Blanco 4 m telescope at Cerro Tololo Inter-American Observatory in Chile in 2018 May as part of the "Mapping Dust in 3D with DECam: A Galactic Plane Survey" (Prop. ID 2018A-0251, PI D. Finkbeiner) from the NOAO Data Lab. We also obtained archival JHK_S data from the Two Micron All-Sky Survey (2MASS) and in the W1 and W2 filters from the Wide-field Infrared Survey Explorer (WISE; Wright et al. 2010) AllWISE data release (Cutri et al. 2013). The host is not detected in archival data from, or was not previously observed by, the Galaxy Evolution Explorer, Spitzer, Herschel, the Hubble Space Telescope (HST), the Chandra X-ray Observatory, the X-ray Multi-Mirror Mission (XMM-Newton), or the Very Large Array Faint Images of the Radio Sky at Twenty-cm survey.

The field of the host is heavily contaminated by galactic sources, including two bright stars located off each end of the host galaxy's disk and four stars located in front of the host. While the four stars obstructing the host do not appear to contribute significant flux to the infrared (IR) data, the two nearby bright stars contaminate the 2MASS and AllWISE catalog magnitudes. To avoid contamination from these sources and obtain IR magnitudes of the host galaxy, we downloaded the JHK_S 2MASS images and measured $5\farcs0$ aperture magnitudes in each filter. Unfortunately, we were unable to perform a similar analysis with the WISE data, as one of the bright stars was too bright to separate from the host galaxy.

In the *gri* DECam data, the stars in front of the host contribute a significant amount of flux, and we cannot measure the host flux directly. In order to obtain an estimate of the uncontaminated host flux in these filters, we used GALFIT (Peng et al. 2002) to determine the flux of the host galaxy. Neighboring and obstructing stars were simultaneously included in the fit. SExtractor (Bertin & Arnouts 1996) was run on each band in order to measure object positions and magnitudes, which serve as initial guesses for GALFIT. A nearby, isolated, bright star was used as a point-spread function (PSF) model, and we tested the results with a second PSF star, finding that the resulting galaxy parameters were consistent.

[26] https://wis-tns.weizmann.ac.il/object/2018dyb

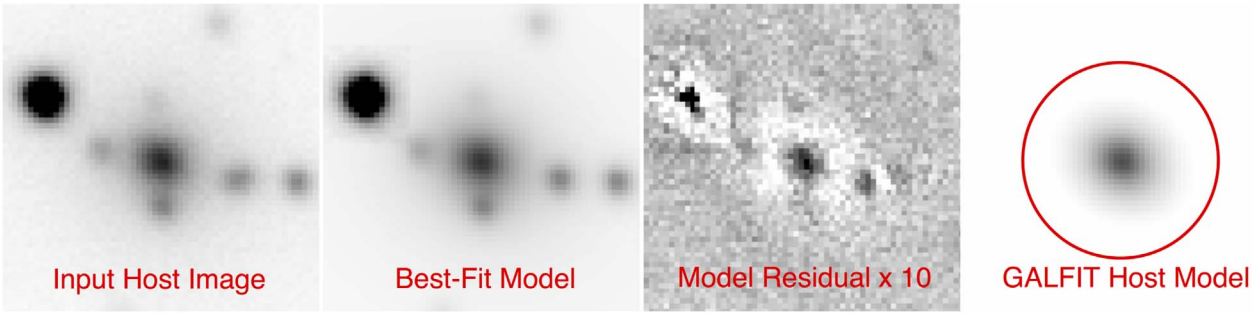

Figure 1. Left panel: DECam *g*-band image of WKK 6047 and nearby stars. Center-left panel: Best-fit star+galaxy model from GALFIT. Center-right panel: Residuals of the model. Residuals have been increased by a factor of 10 to make them more visible, and the difference between the maximum and minimum residuals is approximately 280 counts. Right panel: GALFIT model of the host galaxy isolated from nearby stars. Red circle shows the aperture used to measure an aperture magnitude of the host, and has a radius equal to the *g*-band effective radius of the galaxy. All four images use the same scaling.

The sky mode was measured in each band following Patel et al. (2017) and used as a fixed estimate of the sky background. While the best-fitting Sérsic index n, half-light radius R_e, and total magnitude are sensitive to the sky measurement (as well as other lingering artifacts in the imaging), the flux within $R < n \times R_e$ is fairly stable. We therefore use the best-fitting Sérsic model for the TDE host galaxy to carry out aperture photometry using the effective radius of the host in each filter as the aperture radius, resulting in a robust measurement of the galaxy magnitudes. Aperture photometry was computed for each model image using the IRAF (Tody 1986, 1993) `apphot` package, with the magnitudes being calibrated using multiple stars in the field of the host galaxy with known magnitudes in the AAVSO Photometric All-Sky Survey (APASS; Henden et al. 2015). The input DECam *g*-band data, GALFIT galaxy +star model, model residuals, and isolated galaxy model are shown in Figure 1, with the aperture used to measure the host magnitude shown in the right panel. We list the estimated $griJHK_S$ magnitudes in Table 1.

After measuring the $griJHK_S$ host magnitudes, we fit a spectral energy distribution (SED) to the host magnitudes using the publicly available Fitting and Assessment of Synthetic Templates (FAST; Kriek et al. 2009) code. This fit assumed a Cardelli et al. (1989) extinction law with $R_V = 3.1$ and a galactic extinction of $A_V = 0.624$ mag (Schlafly & Finkbeiner 2011). We adopted a Salpeter initial mass function, an exponentially declining star formation history, and the Bruzual & Charlot (2003) stellar population models for the fit. In order to estimate the host SED and the uncertainties on its physical parameters more robustly, we generated 1000 realizations of the archival fluxes, perturbed by their respective uncertainties assuming Gaussian errors. We then modeled the host SED for each set of perturbed input fluxes with FAST. The resulting median and 68% confidence intervals on the host parameters are: $M_\star = 1.3^{+0.2}_{-0.2} \times 10^{10}\ M_\odot$, age $= 7.9^{+0.8}_{-2.4}$ Gyr, and an upper limit on the star formation rate SFR $< 6.5 \times 10^{-2}\ M_\odot\ \mathrm{yr}^{-1}$. Scaling the stellar mass using the average stellar-mass-to-bulge-mass ratio from the hosts of ASASSN-14ae, ASASSN-14li, and ASASSN-15oi (Holoien et al. 2014, 2016a, 2016b), as we have done with previous TDEs (e.g., Holoien et al. 2019b), gives an estimated bulge mass of $M_B \simeq 10^{9.5}\ M_\odot$. We then convert this to an estimated black hole mass of $M_{\rm BH} = 10^{6.9}\ M_\odot$ using the $M_B - M_{\rm BH}$ relation from McConnell & Ma (2013). This is comparable to the masses of other TDE host galaxies (e.g., Holoien et al. 2014, 2016a, 2016b; Brown et al. 2017; Wevers et al. 2017; Mockler et al. 2019), and our host mass is consistent with that found by Leloudas et al. (2019).

Table 1
Archival Photometry of WKK 6047

Filter	Magnitude	Magnitude Uncertainty
g	16.58	0.11
r	15.59	0.11
i	15.21	0.11
J	14.36	0.05
H	14.05	0.04
K_S	14.34	0.05

Notes. Archival aperture magnitudes of WKK 6047 measured from the GALFIT host model with aperture radius equal to the effective radius of the galaxy (*gri*) and from 2MASS data with 5.″0 aperture radius (JHK_S). These magnitudes were used as the inputs for host-galaxy SED fitting.

In order to obtain fluxes for the transient with the contributions from the host galaxy and nearby stars removed, we require measurements or estimates of the host and stellar fluxes in each filter contained in the 5.″0 apertures used to measure transient magnitudes in our photometric follow-up campaign. For the *gri* bands, we can measure a 5.″0 host+star aperture magnitude directly from the archival DECam images to measure the total contaminating flux. For the Swift UVOT and *uBV* data, however, we do not have any archival images from which to measure this flux. To estimate the host flux in these filters, we derived synthetic host magnitudes for each photometric band using the 1000 bootstrapped SED fits for the host galaxy. We computed synthetic 5.″0 aperture magnitudes in each of our follow-up filters for each of the 1000 host SEDs, yielding a distribution of synthetic magnitudes for each filter. We then used the median and 68% confidence intervals on the host magnitudes as our host magnitude and uncertainties for each band. Due to the lack of archival UV data for the host galaxy, there is a large uncertainty on the SFR of the host. Because of this, there is an allowed subset of host SEDs that have significantly brighter UV fluxes, resulting in a bright tail in the distributions of the host UV magnitudes. The uncertainties on the synthetic UV host magnitudes that we derive from this bootstrapping process are thus quite large. Our follow-up UV magnitudes taken during our observing campaign are significantly brighter than even the brightest UV host magnitudes from our fits, however, so this uncertainty on the host magnitudes results in only a modest increase in the uncertainties of our UV host-subtracted magnitudes.

Table 2
The 5.″0 Host+Star Aperture Magnitudes

Filter	Magnitude and Uncertainty
UVW2	$23.00^{+0.12}_{-2.28}$
UVM2	$22.94^{+0.15}_{-2.18}$
UVW1	$21.16^{+0.21}_{-1.07}$
$U_{\rm UVOT}$	$18.50^{+0.17}_{-0.17}$
u	$18.40^{+0.13}_{-0.17}$
B	$16.98^{+0.12}_{-0.12}$
g	$16.39^{+0.09}_{-0.09}$
V	$15.98^{+0.09}_{-0.08}$
r	$15.43^{+0.09}_{-0.09}$
i	$15.07^{+0.08}_{-0.08}$

Note. The 5.″0 aperture magnitudes of WKK 6047 and the four contaminating stars contained in the aperture synthesized for the Swift UV+*U* and *uBV* filters as described in Section 2.1 and measured directly for the *gri* filters. All magnitudes are in the AB system.

To estimate the contribution from the four stars contained in our aperture, we transformed the *gri* PSF magnitudes from our GALFIT model using various transforms. For *B*- and *V*-band data, we used the Lupton (2005) conversions to convert the *g* magnitudes and $g-r$ colors into *B* and *V* magnitudes. For *u*-band data, we used the $u-g$ colors of a large sample of stars in SDSS DR14 with $g-r$ and $r-i$ colors similar to those of each contaminating star in order to estimate the $u-g$ color of each of the four stars, and we obtained a *u*-band magnitude from this. As there are no published transformations from the SDSS filters to Swift *U*-band, we assume the stars have the same fluxes and magnitudes in *U* as they do in *u*. Finally, we ignore any contribution from the contaminating stars for the UVOT UV filters, as they do not appear to significantly contaminate the data in any epoch. The combined host+star 5.″0 aperture magnitudes that we later subtracted from our follow-up data are shown for each filter in Table 2.

2.2. ASAS-SN Light Curve

ASAS-SN uses units of four 14 cm telescopes on a common mount to monitor the full visible sky on a rapid cadence to find bright, nearby transients (Shappee et al. 2014; Kochanek et al. 2017). ASAS-SN currently is composed of five units hosted by the Las Cumbres Observatory global telescope network (Brown et al. 2013) in Hawaii, Chile, Texas, and South Africa. New ASAS-SN images are processed using a fully automatic pipeline that incorporates the ISIS image subtraction package (Alard & Lupton 1998; Alard 2000). To obtain photometry of ASASSN-18pg uncontaminated by the host and nearby stars, we constructed a reference image of the host galaxy and surrounding sky for each ASAS-SN unit that could observe it. ASASSN-18pg was discovered when the two original ASAS-SN units were still using *V* filters and the new *g*-band telescopes were still building images for references rather than performing normal survey operations. Because of this, we have several years' worth of data of the field in the *V* band, but no images in the *g* band more than a few weeks prior to discovery, when it is likely the images would contain some transient flux. To construct the *V*-band reference image, we used only data obtained prior to 2018 May 1, and for the *g*-band reference image, we used only data obtained after 2019 April 1, when the transient flux was no longer apparent in our data.

Table 3
Host-Subtracted Photometry of ASASSN-18pg

MJD	Filter	Magnitude	Telescope
58320.07	*i*	$15.59^{+0.19}_{-0.19}$	Swope
58320.58	*i*	$15.40^{+0.18}_{-0.18}$	LCOGT_04m
58322.01	*i*	$15.62^{+0.20}_{-0.20}$	LCOGT_04m
…			
58667.63	*UVW2*	$18.00^{+0.15}_{-0.09}$	Swift
58778.79	*UVW2*	$17.90^{+0.14}_{-0.09}$	Swift
58785.09	*UVW2*	$18.13^{+0.18}_{-0.12}$	Swift

Note. Host-subtracted magnitudes and 3σ upper limits for all photometric follow-up data. The Telescope column indicates the source of the data for each epoch: "ASAS-SN" is used for ASAS-SN survey data, "Swope" is used for data from the 1 m Swope telescope at Las Campanas Observatory, "LCOGT_04m" and "LCOGT_1m" are used for data from the Las Cumbres Observatory 0.4 m and 1 m telescopes, respectively, and "Swift" is used for Swift UVOT data. All measurements have been corrected for galactic extinction and are presented in the AB system.

(This table is available in its entirety in machine-readable form.)

We then used these references to subtract the background and host emission from all science images. We performed aperture photometry on each host-template subtracted image using the IRAF `apphot` package, and calibrated the magnitudes to several stars in the vicinity of the transient with known magnitudes in the APASS (Henden et al. 2015). For some prediscovery epochs, when ASASSN-18pg was still very faint, we stacked several science images to improve the signal-to-noise of our detections. We present the ASAS-SN photometry (detections and 3σ limits) in Table 3 and include them in Figure 2. We use error bars on the *X*-axis to denote the date ranges of epochs that were combined to obtain higher signal-to-noise measurements.

2.3. Swift Observations

Our initial Swift follow-up campaign included 25 epochs of TOO observations between 2018 July 18 and 2018 November 6, when ASASSN-18pg became Sun-constrained. After it re-emerged from behind the Sun, we obtained an additional 28 epochs of observations between 2019 January 22 and 2019 October 29, when it became Sun-constrained again. UVOT observations were obtained in the *V* (5468 Å), *B* (4392 Å), *U* (3465 Å), *UVW1* (2600 Å), *UVM2* (2246 Å), and *UVW2* (1928 Å) filters (Poole et al. 2008) in most epochs, with some epochs having fewer filters, depending on scheduling. Since each epoch contains two observations in each filter, we first combined the two images in every filter using the HEAsoft (HEASARC 2014) software task `uvotimsum`, then extracted counts from the combined images in a 5.″0 radius region using the software task `uvotsource`, using a sky region of $\sim 40.''0$ radius to estimate and subtract the sky background. We calculated magnitudes and fluxes from the UVOT count rates based on the most recent UVOT calibration (Poole et al. 2008; Breeveld et al. 2010).

We assumed a Cardelli et al. (1989) extinction law to correct the UVOT transient, host, and star magnitudes for galactic extinction, then subtracted the 5.″0 host+star fluxes from each observation to isolate the transient flux in each epoch. In order to directly compare the Swift *B*- and *V*-band data to our ground-based observations, we converted the UVOT *B* and *V*

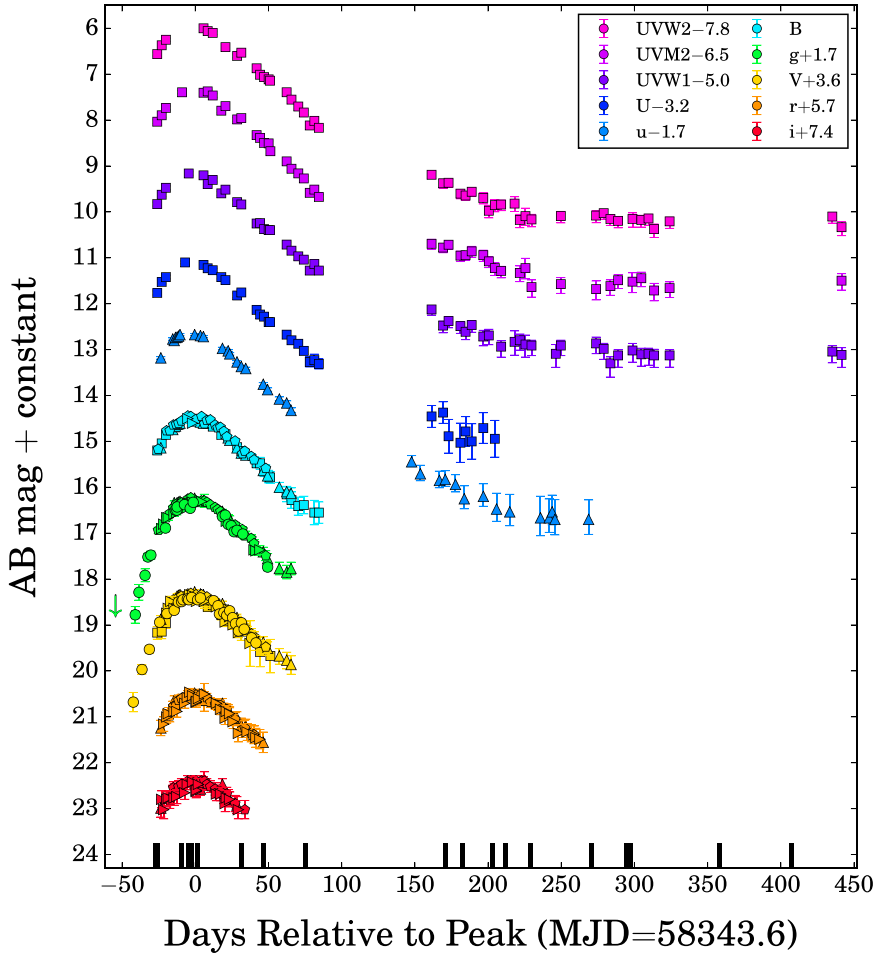

Figure 2. Host-subtracted UV and optical light curves of ASASSN-18pg spanning from 54 days prior to peak brightness (MJD = 58,343.6, measured from the *g*-band light curve; see Section 3.1) to 441 days after peak in the observer frame. ASAS-SN (*gV*) data are shown as circles; Swift UVOT data are shown as squares; and Swope (*uBgVri*), Las Cumbres Observatory 0.4 m (*BVgri*), and Las Cumbres Observatory 1 m (*BVgri*) data are shown as triangles, right-facing triangles, and pentagons, respectively. Downward arrows indicate 3σ upper limits. Early ASAS-SN data have error bars in time to denote the date range of observations that have been combined to obtain a single measurement, though in some cases these error bars may be smaller than the points. Swift *B*- and *V*-band data were converted to Johnson *B* and *V* magnitudes to enable direct comparison with the ground-based data. Black bars along the bottom of the figure show epochs of spectroscopic follow-up. All data have been corrected for galactic extinction and are presented in the AB system.

magnitudes to Johnson *B* and *V* magnitudes using publicly available color corrections.[27] The Swift UVOT photometry are shown in Figure 2 and presented in Table 3.

ASASSN-18pg was also observed using the photon counting mode of Swift's XRT. All observations were reprocessed using the Swift analysis tool `xrtpipeline` version 0.13.2, using the standard filters and screening suggested by the Swift data reduction guide[28] and the most up-to-date CALDB. To place constraints on the presence of X-ray emission arising from ASASSN-18pg, we used a source region centered on the position of ASASSN-18pg with a radius of 30″, and a source-free background region centered at (α, δ) = (16:18:35.3, −61:00:48.4). Similar to Leloudas et al. (2019), we find no significant X-ray emission from the source during its evolution. In order to place the strongest constraints on the X-ray emission arising from ASASSN-18pg, we merged all 54 observations of ASASSN-18pg using `xselect` version 2.4 g. We derived a 3σ upper limit on the count rate of 0.001 counts s^{-1} for the 0.3–10.0 keV energy range. Assuming an absorbed blackbody model with a temperature of 0.05 keV similar to that of other X-ray bright TDEs (e.g., ASASSN-14li, ASASSN-15oi Brown et al. 2016; Holoien et al. 2018) at the redshift of the host galaxy and a galactic column density of 1.77×10^{21} cm^{-2} (HI4PI Collaboration et al. 2016), we obtain an absorbed flux of 2.6×10^{-14} erg cm^{-2} s^{-1}, which corresponds to an upper limit on the X-ray luminosity of $L_X \sim 2 \times 10^{40}$ erg s^{-1}.

We do detect weak ($\sim 2\sigma$ above background) X-ray emission observed during observations ObsID:00010764017 and ObsID:00010764027. Here, we find a background-subtracted count rate in the 0.3–10.0 keV range that has been corrected for encircled energy fraction of 0.004 ± 0.002 count s^{-1} and 0.003 ± 0.001 count s^{-1} for ObsID:00010764017 (+50 days) and ObsID:00010764027 (+169 days), respectively. Given the number of observations, we would expect 1.23 spurious 2σ detections, with a roughly 35% chance of detecting two 2σ detections. The detections in the two epochs where we do detect X-ray emission are slightly greater than 2σ, so the chance that these are both the result of random fluctuations is even lower than this, but we note that it is reasonably possible that there is no actual detected emission from the TDE. However, if we assume they are real detections and use the

[27] https://heasarc.gsfc.nasa.gov/docs/heasarc/caldb/swift/docs/uvot/uvot_caldb_coltrans_02b.pdf
[28] https://swift.gsfc.nasa.gov/analysis/xrt_swguide_v1_2.pdf

Table 4
Spectroscopic Observations of ASASSN-18pg

Date	Telescope	Instrument	Grating	Slit	Exposure Time
2018 Jul 17.15	SOAR 4.1 m	Goodman M1	400 l/mm	1.″00	1 × 900 s
2018 Jul 18.93	SALT 11.1 m	RSS	PG0300	1.″50	1 × 1000 s
2018 Aug 3.86	SALT 11.1 m	RSS	PG0300	1.″50	4 × 900 s
2018 Aug 9.06	du Pont 100 inch	WFCCD	Blue	1.″65	2 × 600 s
2018 Aug 11.05	du Pont 100 inch	WFCCD	Blue	1.″65	2 × 600 s
2018 Aug 15.04	du Pont 100 inch	WFCCD	Blue	1.″65	2 × 600 s
2018 Aug 15.08	Magellan Baade 6.5 m	IMACS $f/2$	300 l/mm	0.″90	3 × 300 s
2018 Sep 13.97	du Pont 100 inch	B and C	300 l/mm	1.″65	3 × 1000 s
2018 Sep 28.00	Gemini South 8.1 m	GMOS	R400	1.″00	2 × 300 s
2018 Oct 28.03	SOAR 4.1 m	Goodman M1+M2	400 l/mm	1.″00	2 × 600 s
2019 Jan 31.36	du Pont 100 inch	WFCCD	Blue	1.″65	3 × 600 s
2019 Feb 12.36	SOAR 4.1 m	Goodman M1	400 l/mm	1.″00	1 × 1200 s
2019 Mar 4.33	du Pont 100 inch	WFCCD	Blue	1.″65	3 × 900 s
2019 Mar 13.32	SOAR 4.1 m	Goodman M1+M2	400 l/mm	1.″00	2 × 1500 s
2019 Mar 28.32	SOAR 4.1 m	Goodman M1+M2	400 l/mm	1.″00	2 × 1800 s
2019 Mar 30.30	Magellan Clay 6.5 m	LDSS-3	VPH-All	1.″00 blue	4 × 600 s
2019 May 11.23	du Pont 100 inch	WFCCD	Blue	1.″65	4 × 1800 s
2019 May 11.29	SOAR 4.1 m	Goodman M2	400 l/mm	1.″00	1 × 1800 s
2019 Jun 4.14	du Pont 100 inch	WFCCD	Blue	1.″65	3 × 900 s
2019 Jun 6.99	SOAR 4.1 m	Goodman M1+M2	400 l/mm	1.″00	2 × 1050 s
2019 Aug 7.04	SOAR 4.1 m	Goodman M1	400 l/mm	1.″00	1 × 1800 s
2019 Sep 24.99	du Pont 100 inch	WFCCD	Blue	1.″65	3 × 1200 s

Note. Date, telescope, instrument, grating, slit size, and exposure time for each of the spectroscopic observations obtained of ASASSN-18pg for the initial classification of the transient and as part of our follow-up campaign.

same absorbed blackbody model that we used to derive the 3σ upper limit from the merged observations, we get an absorbed luminosity of $(9 \pm 5) \times 10^{40}$ erg s^{-1} and $(7 \pm 3) \times 10^{40}$ erg s^{-1}, respectively. This is ∼4 orders of magnitude less than the bolometric luminosity detected at peak. Assuming the BH mass derived in Section 2.1, this suggests that the source is emitting X-rays at only ∼0.01% of Eddington, consistent with what has been found from other X-ray emitting TDEs (e.g., Mockler et al. 2019; Wevers et al. 2019).

2.4. Other Photometric Observations

We also obtained *uBVgri* observations from the Swope 1 m telescope at Las Campanas Observatory and *BVgri* observations from the Las Cumbres Observatory 0.4 and 1 m telescopes located in Cerro Tololo, Chile; Siding Spring, Australia; and Sutherland, South Africa (Brown et al. 2013). We measured 5.″0 aperture magnitudes in these data using the IRAF `apphot` package, using a 13.″0–19.″0 annulus to estimate and subtract background counts while avoiding the nearby contaminating stars. We used several stars in the field with magnitudes available in the APASS DR 10 catalog to calibrate the *BVgri* data. For each comparison star, we estimated a u magnitude by first calculating the average $u - g$ color of a large sample of SDSS DR14 stars with similar $g - r$ colors to the star in question, then assuming this $u - g$ color to estimate a u magnitude using the APASS g-band magnitude. These u magnitudes were then used to calibrate the u-band data.

As with the UVOT observations, we corrected all ground-based aperture magnitudes for galactic extinction and subtracted the flux of the host galaxy and contaminating stars. The host-subtracted ground-based photometry are presented in Table 3 and shown in Figure 2.

2.5. Spectroscopic Observations

We began spectroscopic follow-up observations of ASASSN-18pg following its classification as a possible TDE and continued to monitor it regularly through 2019 September. Our follow-up spectra were obtained with the Robert Stobie Spectrograph (RSS; Burgh et al. 2003) on the 10 m SALT, the Gemini Multi-Object Spectrograph (GMOS; Hook et al. 2004; Gimeno et al. 2016) on the 8.4 m Gemini South telescope, the Inamori-Magellan Areal Camera and Spectrograph (IMACS; Dressler et al. 2011) on the 6.5 m Magellan-Baade telescope, LDSS-3 on the 6.5 m Magellan Clay telescope, the Goodman Spectrograph (Clemens et al. 2004) on the Southern Astrophysical Research (SOAR) 4.1 m telescope, and the Wide Field Reimaging CCD Camera (WFCCD) on the du Pont 100 inch telescope. Our observations span from 26 days prior to peak light through 272 days after and include several spectra taken near or before peak light.

We reduced and calibrated the majority of our spectra using standard IRAF procedures, including bias subtraction, flat fielding, 1D spectrum extraction, and wavelength calibration with an arc lamp taken immediately before or after the science spectra. Most of our observations were then flux calibrated using spectrophotometric standard star spectra obtained on the same night as the science spectra. Spectra obtained with SOAR were flux calibrated using a custom IDL pipeline. Spectra obtained with SALT were reduced in part using the `PySALT` software package (Crawford et al. 2010, 2016). Absolute flux calibration with SALT is difficult because of the telescope design, which has a moving, field-dependent, and underfilled entrance pupil. Observations of spectrophotometric flux standards can, at best, only provide relative flux calibration (see, e.g., Buckley et al. 2018), which mostly accounts for the low-frequency telescope and instrument sensitivity changes as a function of wavelength. We present the details of the spectra in our data set in Table 4.

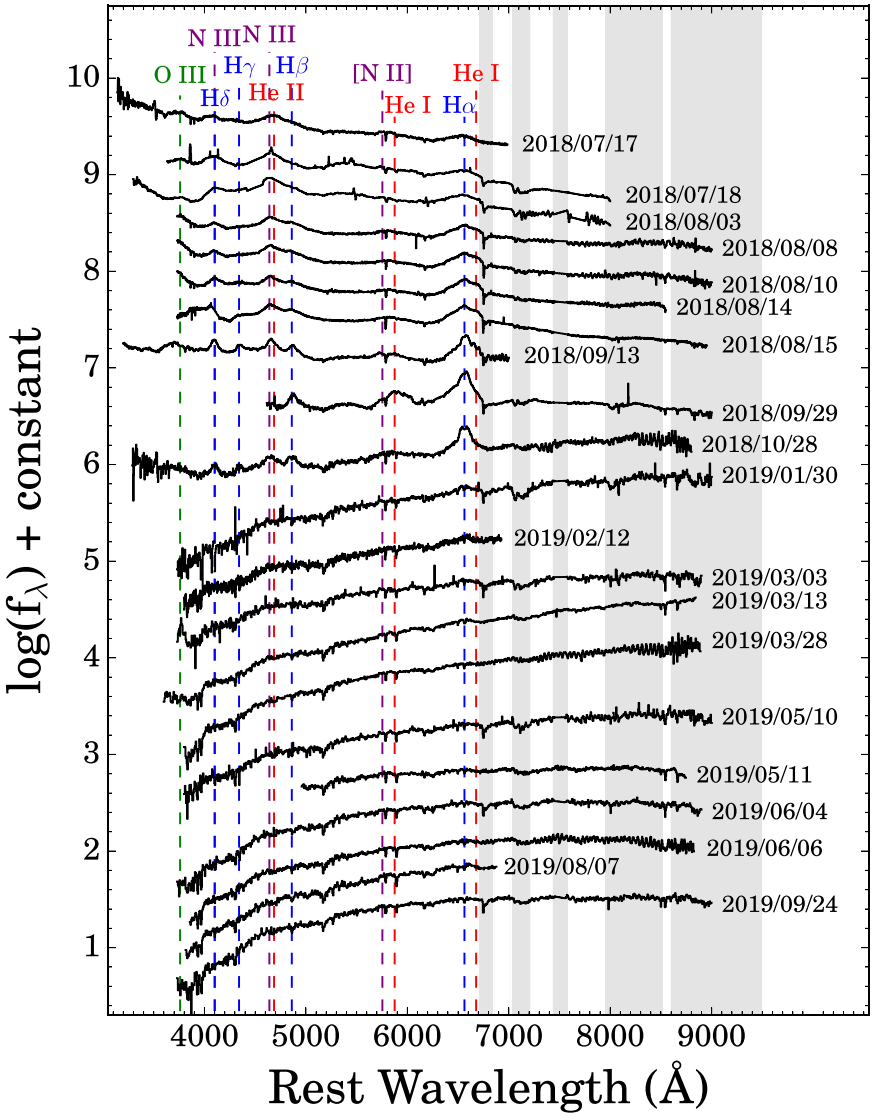

Figure 3. Spectroscopic evolution of ASASSN-18pg spanning from 26 days prior to peak (2018 August 12) through 407 days after peak. As described in Section 2.5, the spectra have been flux calibrated using our photometric observations. Date on which each spectrum was taken is shown to the right of each spectrum, and prominent hydrogen, helium, nitrogen, and oxygen features identified by Leloudas et al. (2019) are indicated with blue, red, purple, and green dashed lines, respectively. Gray-shaded regions indicate telluric bands.

(The data used to create this figure are available.)

We also used our photometric data set to further flux calibrate our spectra. As our spectra were observed through slits of roughly 1.″0 width, we measured magnitudes from our Swope and Las Cumbres Observatory data using a 1.″5 aperture to obtain magnitudes with an amount of host contamination similar to that which would be present in our spectra. For all photometric filters that were completely contained in the wavelength range covered by a given spectrum and for which we could either interpolate the small aperture light curves or extrapolate them by 1 hr or less, we extracted synthetic photometric magnitudes from the spectrum. We then fit a line to the difference between the observed fluxes and the synthetic fluxes as a function of the central filter wavelength and scaled the spectra by the photometric fits. For the two spectra taken in the 2–3 days prior to our first epoch of multiwavelength follow-up observations from Swope, we fit a polynomial to the rising Swope light curves and used these to extrapolate the magnitudes in the Swope filters at the times when our spectra were obtained. We then used the same procedure described above to calibrate the spectra using these extrapolated magnitudes. Finally, we corrected the spectra for galactic extinction using a Milky Way extinction curve, assuming $R_V = 3.1$ and $A_V = 0.624$ (Schlafly & Finkbeiner 2011).

Our final calibrated spectra of ASASSN-18pg are shown in Figure 3. We also mark prominent telluric bands in the figure and have masked the telluric feature from 7550 to 7720 Å and chip gaps (where present). Unlike what was seen in PS18kh (Holoien et al. 2019b) and ASASSN-19bt (Holoien et al. 2019a), where the broad lines did not form until the TDEs were at or near peak light, ASASSN-18pg exhibited broad lines in all spectra taken prior to peak. This may indicate that the lines are being generated through different physical processes in ASASSN-18pg, and we further analyze the line emission in Section 4.

Our second SALT spectrum, obtained on 2018 August 3, was a low-resolution (PG 0300 grating) spectropolarimetric

observation (Nordsieck et al. 2003) obtained under clear conditions with an average seeing of ∼2.″2. Four 900 s exposures were obtained at four half-wave plate positions (0°, 45°, 22.°5 and 67.°5). The data reductions were carried out using the beta version of polSALT[29] (K. Nordsieck & D. Groenewald 2020, in preparation). The software performs basic image reductions on the raw SALT data, after which the data is then wavelength calibrated. The Stoke Q and U parameters, the magnitude of the linear polarization, p, and the position angle of the E-vector, θ, are then determined. This is the first reported spectropolarimetric observation of a TDE, and we discuss the results further in Section 4.2.

2.6. Radio Observations

We observed ASASSN-18pg using the Australia Telescope Compact Array (ATCA) in the 15 mm band, using the Compact Array Broadband Backend (Wilson et al. 2011) to provide 2 × 2048 MHz of bandwidth, centered at 16.7 and 21.2 GHz. Our initial observation was made on 2018 July 20 (08:18–13:29 UT), with the array in its compact H75 configuration, with the inner five antennas all within 90 m, and the sixth antenna separated by 6 km.

We used the standard flux density calibrator PKS B1934−638 to calibrate the bandpass and set the amplitude scale, and the nearby calibrator 1613−586 to solve for the complex antenna gains as a function of time. We reduced the data using standard procedures within the Common Astronomy Software Application (CASA; McMullin et al. 2007). We imaged the data using Briggs weighting with a robustness parameter of 1, as a compromise between sensitivity and resolution. We reached an image noise level of 12 μJy beam^{-1} by stacking both frequency bands. While the source position was coincident with a 50 μJy beam^{-1} peak in the image, it was close enough to a brighter (0.7 mJy) nearby source at coordinates (α, δ) = (16:10:54.52, −60:56:04.8) that it could potentially be attributed to sidelobe confusion in this compact configuration, especially given its marginal (<5σ) significance.

To verify whether or not this marginal detection was real, we made a second ATCA observation on 2018 August 6 (12:20–17:18 UT), with the array in a more extended 1.5 km configuration, providing significantly improved resolution to distinguish the target from the nearby confusing source. We used the same observational setup and data analysis procedures, and did not detect a source at the target position down to a 3σ upper limit of 43 μJy beam^{-1}. We therefore conclude that ASASSN-18pg was not detected in the radio. We note, however, that both of these observations were taken prior to ASASSN-18pg reaching its peak brightness (see Section 3.1), so it is possible that the TDE could have exhibited radio emission at later times that was not detectable prior to peak.

3. Photometric Analysis

3.1. Position, Redshift, and t_{Peak} Measurements

In order to measure the position of ASASSN-18pg, we first generated an image of the TDE by subtracting a g-band image from the Las Cumbres Observatory 1 m telescopes taken in 2019 July from a similar g-band image taken near peak. Using the IRAF task imcentroid, we then measured a centroid position of the TDE flux in the subtracted image as well as the centroid position of the host galaxy nucleus in the archival g-band DECam image. The resulting position of ASASSN-18pg is (α, δ) = (16:10:58.89, −60:55:24.18), which is offset by 0.″20 from the position of the host measured in the archival image. This offset is likely dominated by systematic offset in the astrometry between the two images. To account for this, we also measured the centroid positions of several stars in both the presubtracted, peak g-band image and the archival host image. We then calculated an average offset for the positions of these comparison stars of 0.″24, with the stars being offset in various directions. Thus, the TDE is offset by 0.″20 ± 0.″24 from its host, corresponding to a physical offset of 75.9 ± 91.1 pc.

The redshift of WKK 6047 was reported by Woudt et al. (2008) as $z = 0.017932$. We also measured the redshift of the TDE using the Ca II H and K absorption features that are visible in the 2018 August 15 IMACS spectrum, finding $z = 0.018$. As this is consistent with the Woudt et al. (2008) measurement, we adopt the archival $z = 0.017932$ throughout the manuscript. This corresponds to a luminosity distance of $d = 78.6$ Mpc ($H_0 = 69.6$ km s^{-1} Mpc^{-1}, $\Omega_M = 0.29$, and $\Omega_\Lambda = 0.71$).

To estimate the time of peak light, we used the g-band light curve, which has the best sampling across the peak. We fit a parabola to the host-subtracted data from ASAS-SN and other ground-based telescopes taken between MJD = 58,320 and MJD = 58,370, as the declining light curve is flatter than the rising light curve, making a parabolic fit to the entire light curve impossible. To estimate the uncertainty on the peak time, we generated 10,000 g-band light curves for our specified date range with each magnitude perturbed by its uncertainty, assuming Gaussian errors. We then used a parabolic fit to fit each of these 10,000 light curves and calculated the 68% confidence interval from each of these realizations. Based on this, we find $t_{g,\rm peak} = 58{,}343.6 \pm 0.3$ and $m_{g,\rm peak} = 14.6$. Using the same procedure to calculate the peak times for each of our photometric filters, we find there is some evidence that the redder filters peaked later than the bluer filters, with $t_{\rm UVW2,peak} = 58{,}340.8 \pm 0.4$ and $t_{i,\rm peak} = 58{,}345.2 \pm 1.3$, similar to other TDEs (e.g., Holoien et al. 2018, 2019b; Hinkle et al. 2020b). As the g-band light curve is the best-sampled (due to the ASAS-SN survey data in addition to our high-cadence follow-up data), we adopt a g-band peak of $t_{g,\rm peak} = 58{,}343.6$, corresponding to 2018 August 13.6, throughout our analysis.

3.2. MOSFiT Light Curve Analysis

In order to extract physical parameters of ASASSN-18pg from our photometric data set, we fit the multiband host-subtracted light curves of the TDE using the Modular Open-Source Fitter for Transients (MOSFiT; Guillochon et al. 2017). MOSFiT generates bolometric light curves of transients using models that contain several physical parameters, uses these bolometric light curves to generate single-filter light curves, and fits these to the observed data. It then uses one of various sampling methods to find the combination of parameters that yield the highest likelihood match for a given model. We used the built-in TDE model to fit the light curves of ASASSN-18pg, and due to the large number of photometric filters and observations in our data set, we ran MOSFiT in nested sampling mode for our fits. More details on MOSFiT and specifics on its TDE model can be found in Guillochon et al. (2017) and Mockler et al. (2019).

[29] https://github.com/saltastro/polsalt

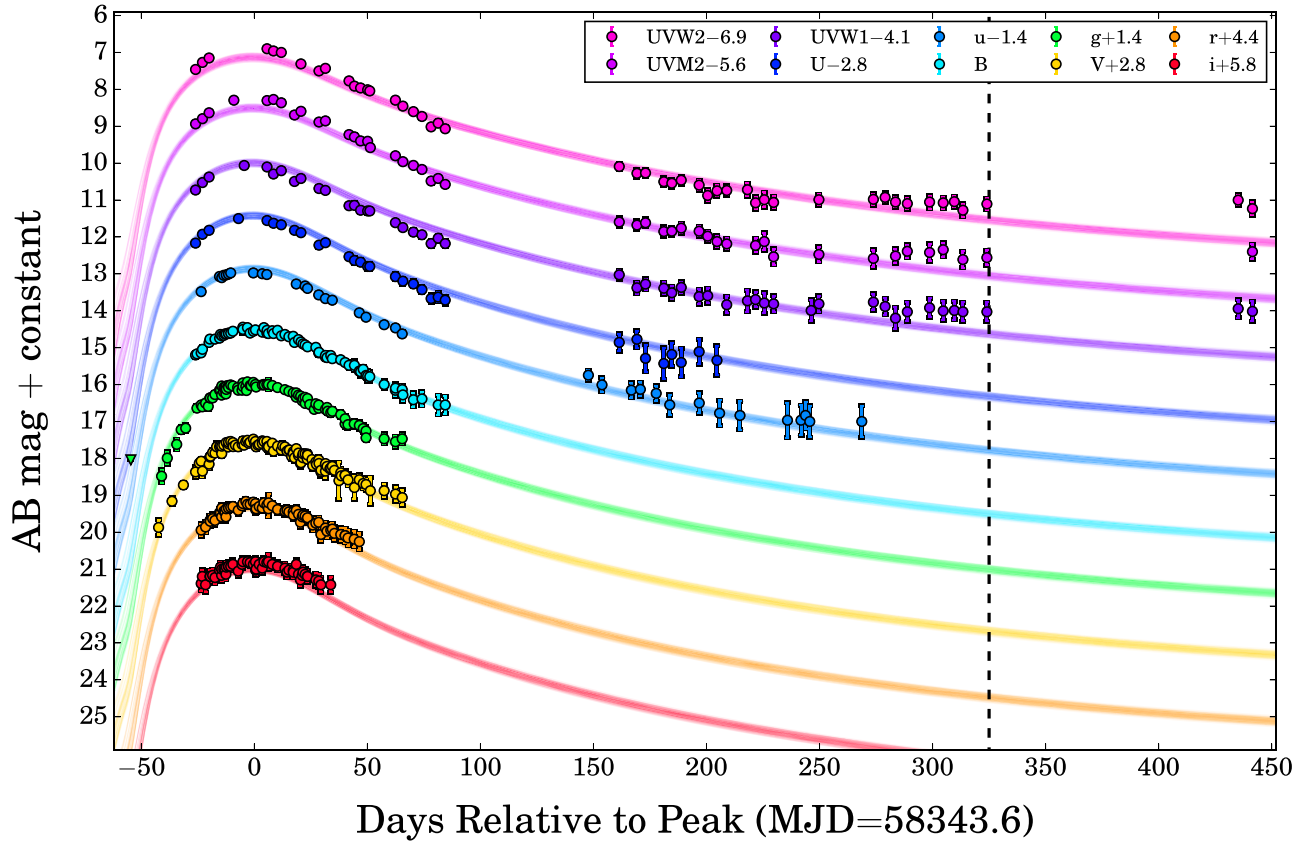

Figure 4. Multiband light-curve fits from MOSFiT with the host-subtracted light curves overplotted. Both the fits and data are plotted in the observed frame. The fits shown represent the 1%–99% range of fits for each filter. Detections are shown as circles and 3σ upper limits are shown with downward triangles, and colors match those of Figure 2. Data to the right of the dashed line were not included when performing the fit, as described in the text.

While the MOSFiT TDE model lacks some physical parameters, such as an accretion disk module that can explain X-ray emission, it is the only tool available for generalized fitting of TDE emission, and works well for modeling cases such as ASASSN-18pg, where the light curves evolve smoothly and there is no X-ray emission. The MOSFiT multiband fits to the ASASSN-18pg light curves are shown in Figure 4 with our data overplotted. Our extremely well-sampled light curves of ASASSN-18pg provide an excellent input data set, and the MOSFiT fits match both the early- and late-time data fairly well, though the fits do underpredict the emission in our latest epochs of observation. Comparing to the fits of several previous TDE discoveries in Mockler et al. (2019), the rise of ASASSN-18pg is much better constrained than the majority of the TDEs in their sample, as we have significantly more data prior to and around peak light.

When fitting the MOSFiT model, we only included observations obtained up to 325 days after peak. We found that when the latest few observations were included in the fits, the late-time data were better fit, but that the rising and peak parts of the light curve were fit significantly worse. Because the rise is so well-constrained by our data, we expect that the most likely explanation for MOSFiT being unable to fit both the early- and late-time data is that either our host flux subtraction method is slightly underpredicting the host emission, resulting in some host contamination that becomes more apparent as the transient emission fades, or that the MOSFiT TDE model does not incorporate the physical components needed to fit both the early- and late-time data simultaneously. Recent studies of TDEs (e.g., Brown et al. 2017; Holoien et al. 2018; van Velzen et al. 2019) have shown that the UV and bluer bands often flatten at later times, which has been attributed to a transition from fallback-dominated to disk-dominated emission. The MOSFiT TDE model was built to predict TDE emission when the bolometric luminosity closely follows the fallback rate, which is likely why it has trouble fitting the data at late times, when this is not necessarily the case. Therefore, we prioritized fitting the early-time data well over the late-time data.

Table 5 shows the median values and 1%–99% range for all the parameters of the MOSFiT TDE model. The model parameters are in general very well-constrained, with the results suggesting that the star almost certainly was completely disrupted in the encounter. We note that the values reported in Table 5 include systematic uncertainties (see Table 3 of Mockler et al. 2019), and that in general the systematic uncertainties on the model parameters are much larger than the uncertainties from the fit.

After accounting for systematic uncertainties, the black hole mass is $M_{\rm BH} = 1.6^{+1.1}_{-0.7} \times 10^7\ M_\odot$, consistent with our estimate based on the stellar luminosity of the host in Section 2.1. The mass of the disrupted star is $M_\star = 0.10^{+0.36}_{-0.08}\ M_\odot$, which is low but consistent with that of several other TDEs in Mockler et al. (2019). This is of interest, as TDEs should occur more frequently with stars of $M \lesssim 0.3\ M_\odot$ (Kochanek 2016).

To test the robustness of this fit, we also performed fits with the same data while adjusting the maximum photosphere size

Table 5
MOSFiT Model Parameter Fits

Quantity	Value	Units
$\log R_{\rm ph0}$	$1.20^{+0.51}_{-0.50}$	...
l (photosphere exponent)	$1.99^{+0.25}_{-0.26}$	...
$t_{\rm fb}$	$-22.64^{+16.33}_{-16.44}$	days
$\log T_{\rm viscous}$	$-0.34^{+0.63}_{-1.25}$	days
b (scaled β)	$1.01^{+0.24}_{-0.84}$	...
$\log M_{\rm BH}$	$7.21^{+0.23}_{-0.24}$	$M_\odot$
$M_\star$	$0.10^{+0.36}_{-0.08}$	$M_\odot$
$\log \epsilon$ (efficiency)	$-0.89^{+0.74}_{-0.74}$	...
$\log n_{\rm H,host}$	$20.67^{+0.03}_{-0.03}$	cm^{-2}
$\log \sigma$	$-0.99^{+0.02}_{-0.02}$	...

Notes. Best-fit TDE model parameters from MOSFiT and 1%–99% range on the uncertainties. Units are listed where appropriate. The uncertainties shown include the systematic uncertainties from Table 3 of Mockler et al. (2019). From top to bottom, the MOSFiT TDE model parameters are: the photosphere power law normalization, the photosphere power-law exponent, the time of first fallback, the viscous timescale, the scaled impact parameter, the black hole mass, the mass of the disrupted star, the efficiency at which material falling onto the black hole is converted to bolometric flux, the column density of the host, and the model variance parameter. These are described in more detail in Mockler et al. (2019).

and the Eddington limit. Altering these parameters did not significantly affect the black hole mass, but did result in some changes to the photosphere parameters, an increase in the stellar mass, and a decrease in the efficiency. The systematic errors from MOSFiT are thus likely the primary source of uncertainty for these parameters of the model.

Leloudas et al. (2019) performed a similar fit with MOSFiT using only the early-time Swift UV data and found best-fit values of $M_{\rm BH} = 4^{+5}_{-2} \times 10^6\ M_\odot$and $M_\star = 0.7^{+4.0}_{-0.6}\ M_\odot$, marginally consistent with our results, although our results are significantly better constrained. We performed fits using both the same epochs of UV data used by Leloudas et al. (2019) and our full UV data set without any optical data. In the former case, we found that the mass was $M_{\rm BH} = 7.8^{+8.8}_{-4.1} \times 10^6\ M_\odot$, and in the latter, the mass was $M_{\rm BH} = 1.1^{+1.1}_{-0.5} \times 10^7\ M_\odot$. While the black hole mass from our fit with the same UV data as Leloudas et al. (2019) is substantially higher than theirs, it is consistent with their black hole mass within uncertainties. In a private communication with G. Leloudas, we discovered a 0.2–0.3 mag difference (a difference of roughly ∼10%) in the galactic extinction applied to correct the UV filters, with our calculated extinction values resulting in brighter magnitudes. This is likely the source of the bulk of the discrepancy between our fits using the same epochs of Swift data.

Leloudas et al. (2019) also estimated the black hole mass using the $M - \sigma$ relation, finding $M_{\rm BH} = 3.3^{+5.0}_{-2.0} \times 10^6\ M_\odot$. As noted in Mockler et al. (2019), MOSFiT generally fits larger black hole masses than the $M - \sigma$ relation, and this is true for the host of ASASSN-18pg as well. However, Mockler et al. (2019) discuss several reasons for this, most notably that the $M - \sigma$ relations in the literature are generally based on galaxies with higher black hole masses and velocity dispersions, and there is significant inherent scatter at the masses and velocity dispersions typically seen in TDE host galaxies. For these reasons, we believe the larger black hole masses that we estimate from MOSFiT and the $M - L$ relation are more likely to be correct for the host of ASASSN-18pg.

The addition of the high-cadence optical data provides useful constraints on the rise time. This lowers the uncertainties on several physical quantities associated with the rising part of the light curve, in particular the star and black hole masses. This highlights the need for both UV and optical monitoring prior to peak light to properly constrain these parameters with tools like MOSFiT.

3.3. SED Analysis

As we have done with previous TDEs (e.g., Holoien et al. 2019a, 2019b), we modeled the UV and optical SED of ASASSN-18pg as a blackbody for epochs where Swift data were available. We fit the SED using a flat temperature prior of 10,000 K $\leqslant T \leqslant$ 55,000 K and used Markov Chain Monte Carlo methods to fit the blackbody SED to the data in each epoch. We then estimated the bolometric luminosity, temperature, and radius of ASASSN-18pg in each epoch from the SED fits.

To get a better picture of the overall evolution of the bolometric luminosity, and to leverage the high-cadence light curves from ASAS-SN, Swope, and the Las Cumbres Observatory 1 m telescopes, we calculated bolometric corrections to the g-band light curve by linearly interpolating between the previous and next g-band measurements bracketing each Swift observation. We then used these bolometric corrections to estimate the bolometric luminosity of ASASSN-18pg from the full g-band light curve by linearly interpolating the bolometric corrections calculated for each Swift epoch to each epoch of g-band data. We used the bolometric correction from the first epoch of Swift SED fits to correct data taken prior to the first Swift observation. The full bolometric luminosity evolution calculated from the SED fits and the bolometrically corrected g data is shown in Figure 5.

We fit the declining bolometric light curve ($t > 30$ days after peak) with several profiles that have been used to fit declining TDE light curves in the past (e.g., Holoien et al. 2019b), including an exponential profile $L = L_0 e^{-(t-t_0)/\tau}$, a $L = L_0(t - t_0)^{-5/3}$ power-law profile, and a power law where the power-law index is allowed to vary, $L \propto (t - t_0)^{-\alpha}$. We chose to limit the fits to $t > 30$ days after peak as the bolometric light curve exhibits a sort of plateau or decline-plus-rebrightening phase over the first ∼30 days after peak, which made it difficult to fit both this period and the later epochs with a single model. We also restricted the t_0 parameter for all three fits to be 22.6 days prior to peak (the time of first fallback fit by MOSFiT), as allowing this to be free is not realistic and results in poor power-law fits. For the exponential profile, we obtain best-fit parameters of $L_0 = 10^{44.2}$ erg s^{-1}, $t_0 = 58{,}375.3$, and $\tau = 52.5$ days; for the $t^{-5/3}$ power law, we obtain $L_0 = 10^{46.8}$ erg s^{-1} and $t_0 = 58{,}343.1$; and for the free power law, we obtain $L_0 = 10^{48.2}$ erg s^{-1}, $t_0 = 58{,}321.0$, and $\alpha = 2.3$. All three fits are shown in Figure 5.

The exponential, free power-law, and $t^{-5/3}$ power-law models have reduced χ^2 values of $\chi^2_\nu = 0.34$, $\chi^2_\nu = 0.46$, and $\chi^2_\nu = 0.64$, respectively. This indicates that all three models overfit the data somewhat, and that all three appear to be reasonable fits to the data, with no strong preference for any of the models over the others. The parameters of the exponential and $t^{-5/3}$ profiles are similar to those of other TDEs fit with the same procedure (e.g., Holoien et al. 2019b), but the free power law is quite a bit steeper than previous results. We find that the best-fit power-law index is highly sensitive to the constraint on the t_0 parameter, as the model

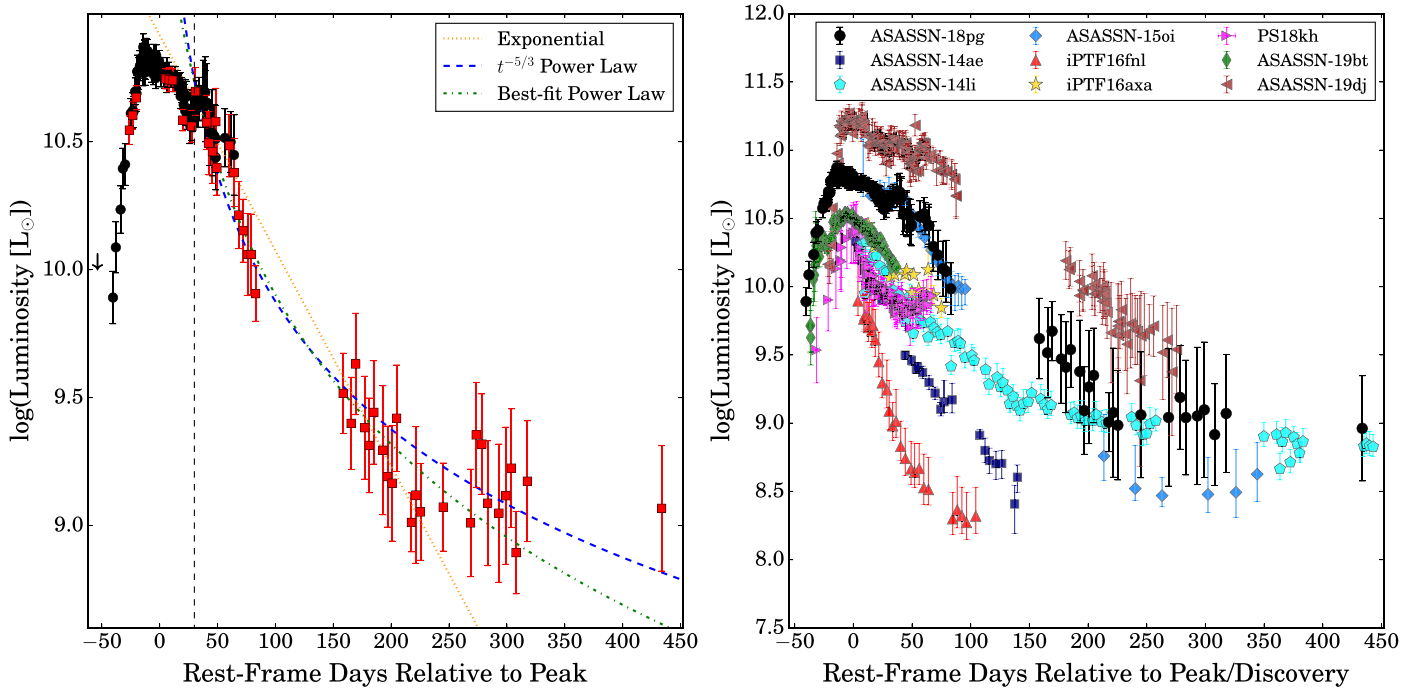

Figure 5. Left panel: Evolution of the UV/optical luminosity of ASASSN-18pg from blackbody fits to the Swift SED (red squares) and *g*-band data that has been bolometrically corrected using the Swift fits (black circles). Downward arrows indicate upper limits. Yellow dotted, blue dashed, and green dashed–dotted lines show exponential, $t^{-5/3}$ power-law, and $t^{-\alpha}$ power-law fits to the declining light curve ($t > 30$ days after peak, indicated by the vertical dashed line), respectively. Right panel: Comparison of the luminosity evolution of ASASSN-18pg to the luminosity evolutions of several other TDEs. Time is given in rest-frame days relative to peak for TDEs that have observations spanning the peak of the light curve (ASASSN-18pg, ASASSN-19bt, ASASSN-19dj, PS18kh, and iPTF16fnl) and in rest-frame days relative to discovery for TDEs that do not (ASASSN-14ae, ASASSN-14li, ASASSN-15oi, and iPTF16axa). Luminosities shown do not include any X-ray contribution, which may be significant in some cases, but is likely associated with a different emission region than the UV/optical emission (e.g., Dai et al. 2018).

prefers to fit the observations to the tail of the power law. This is likely due to the higher time sampling and lower uncertainties for the luminosities closer to peak, both of which result in the model prioritizing fitting the early-time observations over the late-time observations. If t_0 is held close to peak, the best-fit power-law index is close to $\alpha = 5/3$.

Neither the exponential nor the free power-law profiles fit the late-time data as well as the $t^{-5/3}$ power law, and even the $t^{-5/3}$ power law underestimates the luminosity in the latest epochs. Recent theoretical work predicts that there might be a transition in the dominant emission mechanism during TDE flares, with early, fallback-dominated emission following a steeper decline and later disk-dominated emission following a shallower power-law decline (e.g., Lodato & Rossi 2011; Auchettl et al. 2017). It is clear that none of the single models shown in Figure 5 can fit the entire declining period perfectly, implying multiple physical processes are likely contributing to the observed emission. However, the $t^{-5/3}$ profile does fairly well and the best-fit t_0 is very close to our estimated peak date, which suggests that the emission from ASASSN-18pg may be largely fallback-dominated during the duration of our observations.

The right panel of Figure 5 shows the luminosity evolution of ASASSN-18pg compared to several other TDEs from literature: ASASSN-14ae (Holoien et al. 2014), ASASSN-14li (Holoien et al. 2016b), ASASSN-15oi (Holoien et al. 2016a, 2018), iPTF16fnl (Brown et al. 2018), iPTF16axa (Hung et al. 2017), PS18kh (AT 2018zr; Holoien et al. 2019b), ASASSN-19bt (AT 2019ahk; Holoien et al. 2019a), and ASASSN-19dj (AT 2019azh; Hinkle et al. 2020b). The rise of ASASSN-18pg looks generally similar to those of ASASSN-19bt and PS18kh, though it lacks the early luminosity spike seen before peak in ASASSN-19bt (Holoien et al. 2019a). With a peak luminosity of $L_{\rm peak} \simeq 2.4 \times 10^{44}$ erg s^{-1}, ASASSN-18pg is one of the most luminous TDEs in the sample, and it exhibits a period of slower decline following peak that looks very similar to those of ASASSN-15oi and ASASSN-19dj, both of which are also quite luminous. This is consistent with the general finding by Hinkle et al. (2020a) that more luminous TDEs decline more slowly after peak.

Integrating over the rest-frame bolometric light curve, ASASSN-18pg radiated a total of $E = (1.98 \pm 0.08) \times 10^{51}$ erg, with roughly 32% ($(6.40 \pm 0.12) \times 10^{50}$ erg) radiated during the rise to peak. This is significantly more energy output than other recent TDEs (e.g., Holoien et al. 2019a, 2019b), which is not a surprise given the relatively high luminosity and slow post-peak decline exhibited by ASASSN-18pg. An accreted mass of $M_{\rm Acc} \simeq 0.009\eta_{0.1}^{-1}\ M_\odot$, where the accretion efficiency is $\eta = 0.1\eta_{0.1}$, is required to generate the emitted energy. This is very low compared to the mass estimate of the star, as has been seen in other TDEs. ASASSN-18pg thus once again indicates that it is likely only a small fraction of the stellar material actually accretes onto the SMBH during a TDE, or that the radiative efficiency is quite low (e.g., Holoien et al. 2014, 2016b, 2018).

The blackbody temperature evolution of ASASSN-18pg from the Swift fits is shown in Figure 6 along with the evolution for the same comparison sample shown in Figure 5. ASASSN-18pg shows very little temperature evolution throughout the duration of the flare, remaining roughly constant around $T \sim 30{,}000$ K until late times. There is some evidence of a temperature increase/spike around 60 rest-frame days after peak, possibly reaching as high as $T \sim 45{,}000$ K, but the uncertainties are large enough that this spike may not be quite so dramatic. It is clear that ASASSN-18pg does not exhibit any of the more dramatic changes seen in some of the other TDEs,

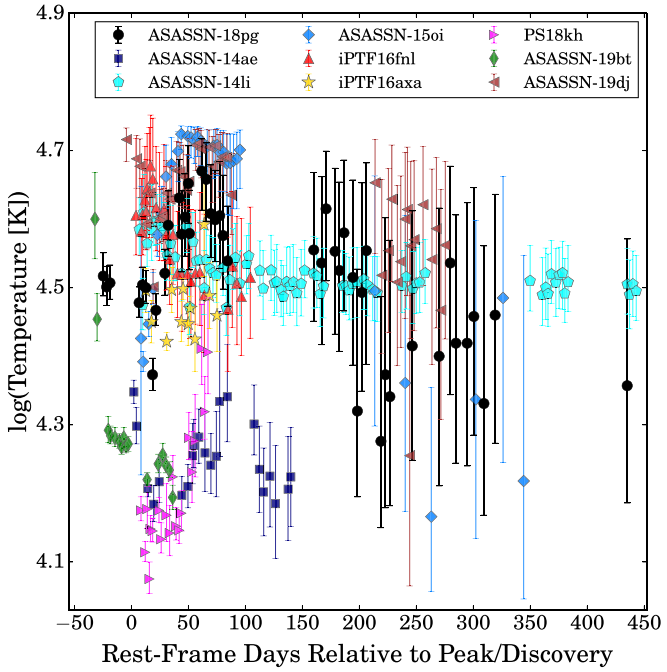

Figure 6. Temperature evolution of ASASSN-18pg from our Swift blackbody fits (black circles) compared to those of the TDE comparison sample. As described in the caption of Figure 5, time is shown in rest-frame days relative to peak or discovery, and symbols and colors match those of Figure 5.

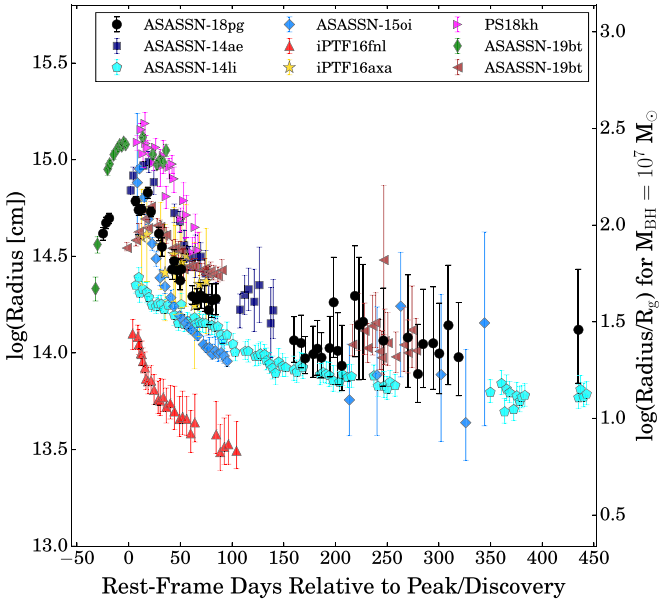

Figure 7. Evolution of the blackbody radius of ASASSN-18pg from the Swift fits compared to those of the TDEs in the comparison sample. As described in the caption of Figure 5, time is shown in rest-frame days relative to peak or discovery, and symbols and colors match those of Figure 5. Sscale on the left shows the radius in units of cm and the scale on the right shows the same scale in units of the gravitational radius for a 10^7 $M_\odot$ black hole.

such as the early temperature drop of ASASSN-19bt (Holoien et al. 2019a), the early rises of ASASSN-15oi and PS18kh (Holoien et al. 2018, 2019b), or the late-time drop of ASASSN-15oi (Holoien et al. 2018). Our Swift observations of ASASSN-18pg cover a long enough time baseline to make comparison at both very early and late times possible, which has not been the case with any other TDE in the sample. The lack of an early drop in the temperature as seen in ASASSN-19bt is of note, as ASASSN-19bt was the first TDE with UV data to fit the blackbody temperature at such early times, and it is unclear how common such an early temperature decline is.

Finally, in Figure 7, we show the evolution of the blackbody radii of ASASSN-18pg and the comparison TDEs. Similar to ASASSN-19bt, the radius increases prior to peak light in ASASSN-18pg, though the rise is considerably slower than that of ASASSN-19bt. Following peak, the radius declines fairly rapidly before leveling off at later times, and appears to be very similar in size and evolution to those of ASASSN-19dj and ASASSN-14ae in particular. In general, the radius evolution of TDEs appears to be much more homogeneous than the temperature or luminosity evolutions, with the majority of the objects in our sample exhibiting similar sizes and evolutions. In general, it seems that TDEs with hotter temperatures have smaller peak radii, but there does not appear to be much difference in the rate of change of the radius with different temperatures. However, few of the TDEs in this sample have both early- and late-time data, making it difficult to draw conclusions about potential trends, particularly past ∼100 days post-peak.

4. Spectroscopic Analysis

4.1. Emission Line Analysis

As noted by Leloudas et al. (2019), ASASSN-18pg is a member of a new class of TDEs that exhibit several emission lines resulting from the Bowen fluorescence mechanism in addition to the broad hydrogen and helium lines common to TDEs. Several other TDEs with similar features have now been identified (Blagorodnova et al. 2019; van Velzen et al. 2020). Many of these lines are clearly detected in several of our spectra, and we fit these features in order to measure the evolution of the lines.

We fit the lines as Gaussian profiles atop a linear continuum. Due to the broadness of the emission profiles and the low signal-to-noise ratio of most of our spectra, we manually selected regions of the spectrum near each line for continuum estimation. The continuum was removed and the remaining emission profiles were fit with three free parameters: velocity width, velocity shift from the rest wavelength, and amplitude of the emission profile. The parameters were initially estimated by manually adjusting the values until a reasonable fit was achieved, followed by using a least-squares minimizer to fine-tune the results. Due to the number of broad emission lines, identifying and removing the proper continuum level is nontrivial and likely contributes $\gtrsim$25% of our overall error budget. For this reason, we focus more on relative changes as ASASSN-18pg evolves, rather than absolute measurements. We only attempt to fit the lines in our spectra taken through the end of 2019 March, as no transient emission line features are detected in our later observations.

The Hα feature starts out as a single, broad Gaussian with width of ∼15,000 km s^{-1} in our early spectra. Over time, a narrow peak (width of ∼6000–7000 km s^{-1}) develops atop the broad Hα. After the narrow feature has appeared, we fit the narrow and broad components simultaneously with Gaussian profiles, as the narrow emission component is narrow enough where the telluric absorption is not an issue. Figure 8 shows the early evolution of the region around Hα with the individual components of our model. The narrow feature appears near peak light and becomes dominant as time progresses, but has

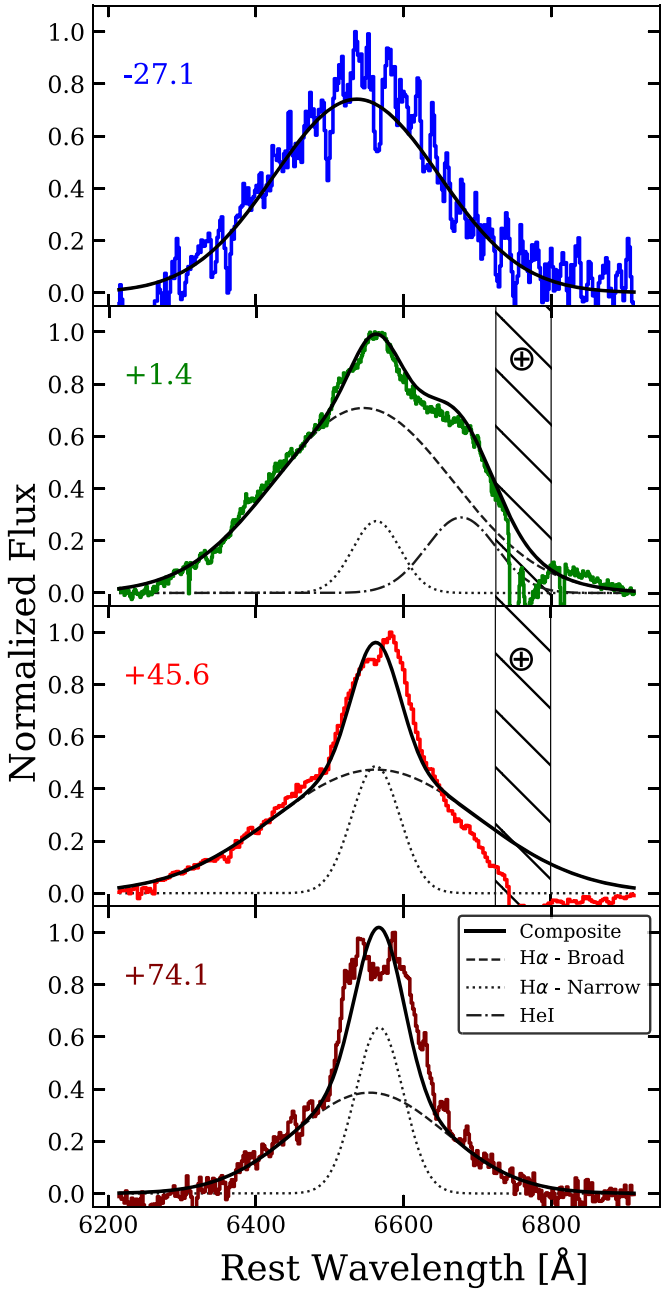

Figure 8. Region around the Hα line and our model fits to several epochs. Gaussians corresponding to the broad Hα, narrow Hα, and He I components of the fit are shown as dashed, dotted, and dashed–dotted lines, respectively, with the composite model shown as a solid line. Hatched region indicates a telluric band that is not included in the fit. Not all components are present in every epoch, and the time relative to peak is shown in the upper left corner of each panel. Hα profile clearly develops a second, narrow component near the time of peak light that becomes stronger over time, and He I is only definitively detected near peak.

disappeared after ASASSN-18pg reappeared from being Sun-constrained.

Due to the heavy telluric contamination between 6830 and 6980 Å (6710–6860 Å rest-frame), decomposing the individual contributions from Hα and He I 6678 Å is nontrivial. When ASASSN-18pg is near peak light, the Hα and He I emission lines are strong enough to provide a general estimate of the properties for both lines (e.g., Figure 9, green spectrum), albeit with large uncertainties. We provide the flux estimates for the He I 6678 Å line in the middle panel of Figure 10, but caution that the uncertain continuum level is a large source of systematic uncertainty. For all other epochs, we only fit the peak and left wing of the Hα profile to estimate emission-line properties.

Overall, our results are consistent with those found by Leloudas et al. (2019), with the exception of the two-component Hα line. No emission lines show any significant deviation from the rest wavelength. The evolution of several continuum-subtracted emission features are shown in Figure 9 and described below, and we show the evolution of the fluxes of the various lines in Figure 10.

The broad Hα component grows broader from 2018 July until 2018 August, with the FWHM increasing from ∼12,000 to ∼15,000 km s^{-1}. The narrow Hα component becomes visible in 2018 August, growing stronger over time and becoming roughly equivalent in strength to the broad component shortly before ASASSN-18pg becomes Sun-constrained in 2018 November. After the TDE has re-emerged from behind the Sun in 2019 January, the broad component is still detected with FWHM ∼ 6000 km s^{-1}, but the narrow component is no longer detected. The broad Hα component becomes fainter over time with similar FWHM, and is no longer detected after 2019 March.

Broad Hβ emission is seen throughout the evolution of the TDE, with the line narrowing from FWHM ∼ 12,000–15,000 km s^{-1} in 2018 July and August to FWHM ∼ 6000–7000 km s^{-1} in 2018 September and October. After re-emerging from being Sun-constrained, the Hβ region is dominated by a complex of lines also including He II 4686 Å and N III 4640 Å lines, and it is difficult to extract each line's individual contributions. Hβ likely continues to be detected until late 2019 March. We do not detect a narrow Hβ line similar to the narrow Hα component in any epoch.

The Hγ line is undetected until the spectrum obtained on 2018 August 14, where we tentatively detect weak Hγ emission with FWHM ∼ 8000 km s^{-1}. It remains detected until the TDE became Sun-constrained, with the emission peaking in strength on 2018 September 13, and is not detected after. The only plausible detection of Hδ occurs on 2018 September 13, when the Hγ emission is strongest, corresponding to a shoulder on the red wing of the N III 4100 Å emission profile (see below).

Weak He I 6678 Å and He II 4686 Å lines become visible in 2018 August and are blended with the Hα and Hβ lines, respectively. The He II 4686 Å line is particularly weak compared to the Hβ and N III 4640 Å lines in the same region of the spectra. He I 6678 Å is not detected after the TDE becomes visible again in 2019, and the He II 4686 Å line is only tentatively detected once at later times.

Similar to Leloudas et al. (2019), we detect a feature near 5800 Å, which was speculated to be a blend of He I 5876 Å and [N II] 5754 Å lines. This region cannot be fit by any reasonable combination of these two line profiles for any of our spectra unless these lines have significant shifts from their rest wavelengths not evident in any of the other emission lines. Significant host galaxy and/or Milky Way Na ID absorption complicates the fitting process. Thus, we conclude that the origin of this emission feature remains ambiguous.

Finally, Leloudas et al. (2019) identified several emission lines seen from ASASSN-18pg as the result of Bowen fluorescence, and van Velzen et al. (2020) have since discovered several other TDEs with similar emission features. We also detect many of these lines in our spectra at various

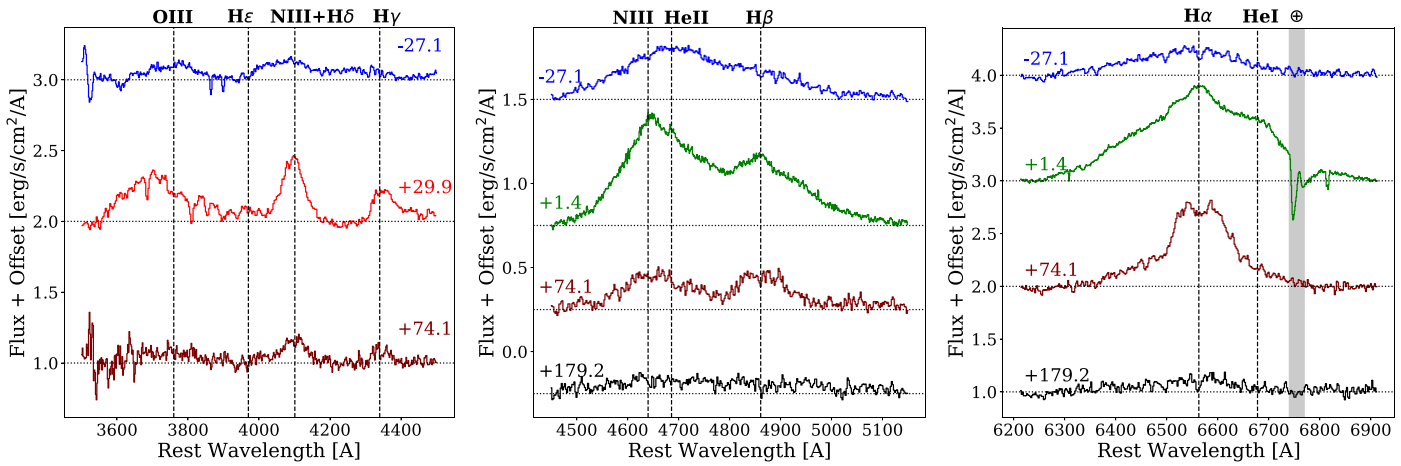

Figure 9. Evolution of the spectroscopic emission features centered on the O III 3760 Å triplet and 4100 Å line complex (left panel), Hβ (center panel), and Hα (right panel). Spectra were chosen to show the lines roughly one month prior to peak, near peak, roughly two months after peak (shortly before it becomes Sun-constrained), and roughly six months after peak, with the epoch in rest-frame days relative to peak shown next to each spectrum. Spectra shown in the left panel differ from those of the other two panels in some cases, as only some of our follow-up spectra cover this wavelength range. Prominent lines are indicated with dashed lines and a linear continuum has been subtracted from each spectrum.

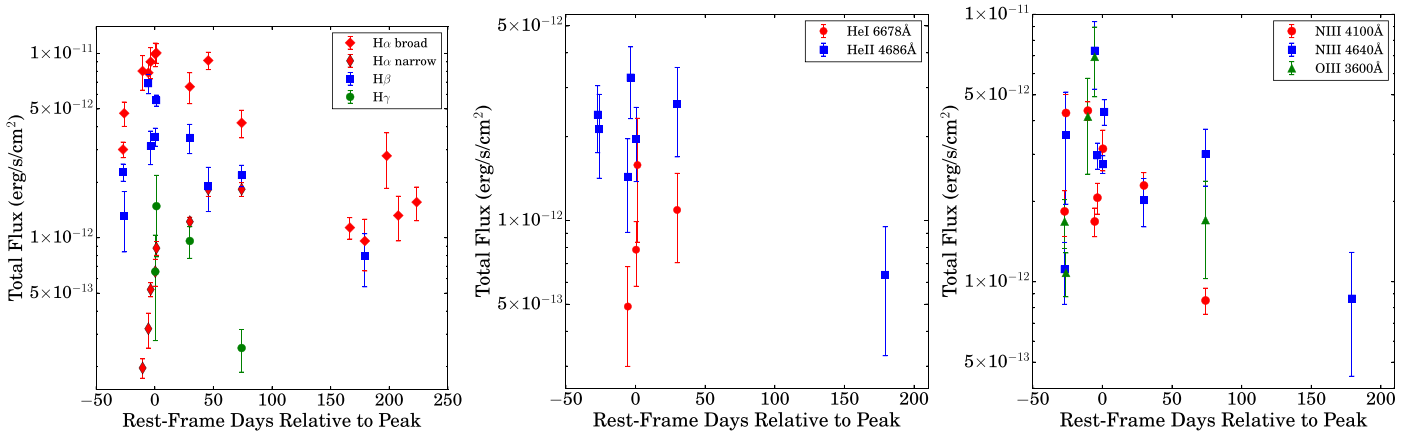

Figure 10. Left panel: Evolution of the fluxes of the Hα broad and narrow components (wide and thin red diamonds, respectively), the Hβ line (blue squares), and the Hγ line (green circles). Center panel: Evolution of the fluxes of the He II 4686 Å (red circles) and He I 6678 Å (blue squares) lines. Right panel: Evolution of the fluxes of the N III 4100 Å (red circles), N III 4640 Å (blue squares), and O III 3600 Å (green triangles) lines.

times. The N III 4640 Å is of similar width and flux to the Hβ line in most epochs, evolving similarly to become stronger and broader for roughly the first month after discovery and remaining detected at late times.

In agreement with Leloudas et al. (2019), we clearly detect the O III 3760 Å triplet and an emission complex near 4100 Å that we consider likely to be N III 4100 Å emission, rather than Hδ. The evolution of the O III 3760 Å line roughly tracks that of N III 4640 Å, while the N III blend begins broad and gradually decreases in amplitude and FWHM over time.

We observe an apparent delay between the times when the broad and narrow Hα components peak. Motivated by this, we examined whether these components could illuminate the geometry of the gas responsible for the spectroscopic features, under the assumption that the line formation physics is similar to that assumed for reverberation mapping studies of quasars (e.g., Peterson et al. 2004). To do this, we first took the bolometric luminosity curve and extrapolated to times earlier than our first detection as a power law. This extrapolation does not strongly affect the resulting light curves as long as there is no unobserved early peak. We then convolved this bolometric curve with the transfer functions of spherical shells of several radii (a top hat from zero to $2R_{\rm shell}/c$). This produced light curves one might expect for the simplistic case of a spherical shell of gas reprocessing some of the UV emission from the TDE into recombination line emission (e.g., Peterson et al. 2004).

In Figure 11, we show the luminosities of the bolometric, broad Hα, and narrow Hα components, each normalized to their maximum values. Overplotted on the data are the spherical shell approximations, running from 5 to 100 lt-day. Though none of the extrapolated curves fit the spectroscopic components exactly, the broad Hα luminosity is roughly consistent with a shell of 5–20 lt-day, while the narrow component is roughly consistent with a shell of 40–60 lt-day. This model is agnostic about the origin of the line-emitting gas, and simply assumes that there are two regions of gas outside the TDE photosphere that are responsible for the two Hα components, analogous to the broad-line and narrow-line regions in active galactic nuclei. Both, either, or neither of these line-emitting regions could be associated with the TDE.

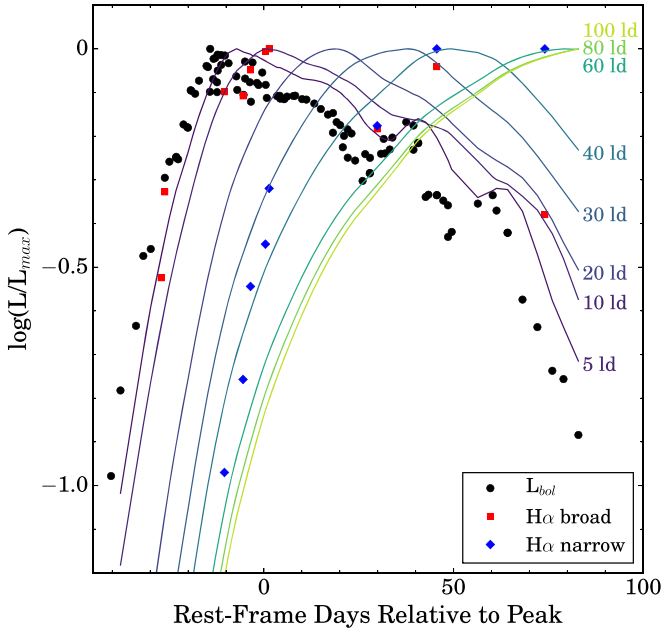

Figure 11. Light curves of the bolometric luminosity (black circles), broad Hα component (red squares), and narrow Hα component (blue diamonds), normalized to the peak luminosity for each. Colored lines show the expected luminosity curves for spherical shells of different radii reprocessing the bolometric emission, with the radius in light days given next to each. Bolometric light curve prior to the first detection was extrapolated as a power law to earlier times, and the delay distribution of each shell is a top hat running from a delay of zero to $2R_{\rm shell}/c$.

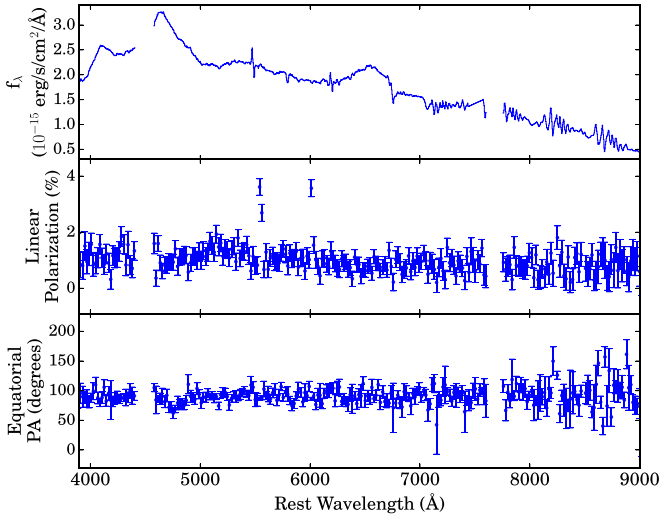

Figure 12. Spectropolarimetric observation of ASASSN-18pg obtained on 2018 August 3 from SALT. Top panel: Photometry-calibrated spectrum, also shown in Figure 3. Middle panel: Linear polarization. Bottom panel: Instrumental equatorial position angle. Both the linear polarization and the position angle have been binned in 20 Å bins to increase readability. We do not display observations at wavelengths shorter than 4000 Å or longer than 9000 Å, where uncertainties on the polarization and position angle are large.

The geometry of reprocessing gas is likely much more complicated than a simple spherical shell, and is also likely evolving on fairly rapid timescales, but the fact that these simple approximations can reasonably fit the data implies that these spectroscopic features are likely coming from different regions around the black hole, with the narrow component likely being significantly more distant and slower-moving than the broad component.

We note that we detect broad emission features in all spectra obtained prior to peak, including our first spectrum obtained approximately 27 rest-frame days before peak. This is in contrast to several other recent TDEs with spectroscopic observations at similar times, such as PS18kh, ASASSN-19bt, and ASASSN-19dj, which exhibited a strong blue continuum but no emission features until closer to peak light (Holoien et al. 2019a, 2019b; Hinkle et al. 2020b). There are roughly 16 rest-frame days between our first detection of the TDE in ASAS-SN data and our first spectrum, so we cannot rule out the possibility that the emission features would not be detected if ASASSN-18pg had been observed earlier. However, if the lines are present in all epochs, this perhaps suggests a different physical origin for these features in ASASSN-18pg than in other TDEs with early observations. In particular, ASASSN-18pg is a Bowen TDE, while PS18kh, ASASSN-19bt, and ASASSN-19dj are all H-rich TDEs. As Bowen fluorescence is a process that requires reprocessing of higher-energy emission, this suggests that the emission features in ASASSN-18pg are driven by reprocessing of emission from the accretion disk, and that the lines are present in all epochs because the UV/optical emission is not detected until the disk emission has been reprocessed (e.g., Roth et al. 2016; Roth & Kasen 2018). If the UV/optical emission in the other TDEs is driven by shocks in the tidal debris stream as it collides with itself (e.g., Piran et al. 2015; Krolik et al. 2016), it is possible we may not observe lines until later times, or see more rapid variation, as the material responsible for the emission is evolving on short timescales. Viewing angle may also play an important role in the observed difference between ASASSN-18pg and these other objects (e.g., Dai et al. 2018). More TDEs with very early-time spectroscopic observations such as these are needed to determine if there truly is a subset of TDEs that exhibit lines in all epochs, and to determine the origin of the different timescales we observe in the emergence of the emission features in TDEs.

4.2. Spectropolarimetry of ASASSN-18pg

As mentioned in Section 2.5, the SALT spectrum obtained on 2018 August 3 was a low-resolution spectropolarimetric observation. Such observations can be useful for determining the geometry of the emission source and may be particularly illuminating for TDEs, which are expected to be quite aspherical and rapidly evolving (e.g., Guillochon & Ramirez-Ruiz 2013, 2015), particularly at times shortly after disruption. These observations were obtained roughly 10 rest-frame days prior to peak, and represent the first published spectropolarimetric observations of a TDE. The spectrum, polarization, and instrumental position angle are shown in Figure 12.

We detect a nominal polarization of ∼1.5% with uncertainties of ∼0.5% that remains roughly constant with some slight variation from 4000 to 9000 Å. We only examine this wavelength range, as uncertainties on the polarization and position angle balloon at shorter and longer wavelengths. We do not see any obvious features in the polarization associated with the emission lines as compared to the continuum, implying that the lines and continuum have a similar projected geometry.

In order to determine whether this polarization is intrinsic to the TDE, we first examine whether the polarization could be

consistent with interstellar polarization (ISP), which is induced by dichroic absorption of the TDE light by interstellar dust grains aligned to the magnetic field of the interstellar medium along the line of sight to the TDE. Due to the high galactic extinction in the direction of the TDE ($E(B-V) \simeq 0.2$ mag), there could be up to $P_{\rm ISP} < 9E(B-V) \simeq 1.8\%$ galactic ISP (Serkowski et al. 1975; Bose et al. 2018), which is consistent with the polarization we measure. Polarization measurements of three stars within 1° of ASASSN-18pg also support this, with the stars having polarization of ∼1% at position angles of ∼50° (Heiles 2000), similar to what we measure in our observation of ASASSN-18pg. Thus, we conclude that the detected polarization is likely due to galactic ISP.

However, if we assume the polarization is intrinsic to the TDE, a polarization of 2% corresponds to an axis ratio in the projected emission region of ∼0.65 and a polarization of 1% corresponds to an axis ratio of ∼0.8, assuming that the Hoflich (1991) analysis for supernovae can be applied to TDEs. Even if all of the polarization is intrinsic to the TDE, these observations imply that the projected emission region is quite spherical compared to the initial planar, elliptical distribution of the stellar debris stream.

5. Summary and Discussion

With several hundred observations spanning from 54 days prior to peak light through 441 days after peak light, our data on ASASSN-18pg represent one of the most comprehensive early-through-late-time data sets available for a TDE. It includes X-ray, UV, optical, and radio observations as well as spectra spanning several hundred days of the TDE's evolution and the first published spectropolarimetric observations of a TDE.

Due to our early discovery and subsequent triggering of additional follow-up resources, our data include multiwavelength data prior to peak spanning from the X-ray through optical wavelengths as well as several spectra taken before and around peak light, allowing us to characterize the early blackbody evolution and spectroscopic evolution of this TDE. Our early photometry provide strong constraints on the rise time, in turn providing good constraints on the black hole mass, star mass, and viscous delays, parameters of the `MOSFiT` model. The blackbody fits indicate that ASASSN-18pg peaked at a luminosity of $L_{\rm peak} \simeq 2.2 \times 10^{44}$ erg s^{-1}, making it one of the more luminous UV/optical TDEs discovered to-date. It declines at a relatively slower rate than less luminous TDEs, and follows the peak luminosity–luminosity decline rate relation discovered by Hinkle et al. (2020a).

ASASSN-18pg is a member of the recently identified class of TDEs that exhibit emission lines attributed to Bowen fluorescence (Leloudas et al. 2019). Unlike other TDEs, which develop emission lines in their spectra at or shortly before peak light (e.g., Holoien et al. 2019a, 2019b), ASASSN-18pg exhibits emission lines in all epochs, including our earliest spectrum obtained 27 rest-frame days before peak. This perhaps suggests that the UV/optical emission is not detected until the lines have formed, implying that the UV/optical emission in ASASSN-18pg may be the result of reprocessing of emission from the accretion disk. However, more TDEs with very early spectra, particularly of the TDE-Bowen class, are needed to see if there truly is a population of TDEs which show lines in all spectra, or whether TDEs simply exhibit lines at different timescales.

Our early observations also include two radio observations from ATCA obtained prior to peak light, roughly two weeks apart. The observations indicate the TDE was not detected in the radio, implying that if the TDE did launch a jet or outflow (e.g., Alexander et al. 2016; van Velzen et al. 2016), it was not visible along our line of sight to the TDE.

Our late-time observations include both spectra and Swift observations obtained over 400 days after peak light. While the blackbody evolution of ASASSN-18pg at late times is consistent with those of other TDEs with similarly late observations, we do not detect X-ray emission in any epoch, nor do we detect any evolution in the X-rays as has been seen in other TDEs (e.g., Gezari et al. 2017; Holoien et al. 2018; Hinkle et al. 2020b; van Velzen et al. 2020). Spectra obtained after 2019 March, roughly nine months after peak light, show no evidence of features related to the TDE, nor is there any significant spectroscopic evolution after this time.

Our data set also includes the first published spectropolarimetric observations of a TDE, obtained roughly 10 rest-frame days prior to peak light. These observations find a polarization consistent with that of nearby stars and the line-of-sight galactic extinction. If we interpret this as a ∼1% upper limit on polarization from the source, this implies that the emission is relatively spherical. Based on the models for SNe Ia by Hoflich (1991), the axis ratio of the projected emission region would have to be $\gtrsim$0.8, or there is little scattering to produce the polarization. There are also no obvious changes in the polarization with wavelength, including any differences between the line and continuum emission. While spectropolarimetric observations are expensive, spectropolarimetry provides the only way of probing the symmetry of the emission, and so might open an important new window into TDE physics. Multiple epochs of spectropolarimetry are important both to look for changes in the symmetry and because changes in polarization can be measured without worrying about the contamination from foreground sources of polarization.

This data set includes not only well-sampled observations after peak, as many UV/optical TDE data sets now do, but also the very early- and late-time data that has traditionally been missing in our observations of TDEs. These data are needed to differentiate between different emission models, and to test theoretical predictions for TDE emission. With surveys like ASAS-SN now finding TDEs earlier and more frequently, ASASSN-18pg should become one of many TDEs with similar data sets, hopefully resulting in a unified model of TDE emission.

We thank Y.-C. Pan, J. Anais Vilchez, A. Campillay, N. Muñoz-Elgueta, N. Ulloa, and J. Vargas-González for contributions to observing for this data set. We thank the referee for helpful comments that improved our analysis and the readability of the paper.

We thank the Las Cumbres Observatory and its staff for its continuing support of the ASAS-SN project. ASAS-SN is supported by the Gordon and Betty Moore Foundation through grant GBMF5490 to the Ohio State University, and NSF grants AST-1515927 and AST-1908570. Development of ASAS-SN has been supported by NSF grant AST-0908816, the Mt. Cuba Astronomical Foundation, the Center for Cosmology and AstroParticle Physics at the Ohio State University, the Chinese

Academy of Sciences South America Center for Astronomy (CAS-SACA), the Villum Foundation, and George Skestos.

K.A.A. is supported by the Danish National Research Foundation (DNRF132). C.S.K. and K.Z.S. are supported by NSF grants AST-1515927 and AST-181440. C.S.K., K.Z.S., and B.J.S. are supported by NSF grant AST-1907570. M.A.T. acknowledges support from the DOE CSGF through grant DE-SC0019323. B.J.S. is also supported by NSF grants AST-1920392 and AST-1911074. Support for J.L.P. is provided in part by FONDECYT through the grant 1151445 and by the Ministry of Economy, Development, and Tourism's Millennium Science Initiative through grant IC120009, awarded to The Millennium Institute of Astrophysics, MAS. T.A.T. is supported in part by Scialog Scholar grant 24215 from the Research Corporation. P.S.C. is grateful for support provided by NASA through the NASA Hubble Fellowship grant #HST-HF2-51404.001 A awarded by the Space Telescope Science Institute, which is operated by the Association of Universities for Research in Astronomy, Inc., for NASA, under contract NAS 5-26555. K.D.F. is supported by Hubble Fellowship grant HST-HF2-51391.001 A, provided by NASA through a grant from the Space Telescope Science Institute (STScI), which is operated by the Association of Universities for Research in Astronomy, Inc., under NASA contract NAS5-26555. D.A.H. B. is supported by the National Research Foundation (NRF) of South Africa. M.G. is supported by the Polish NCN MAESTRO grant 2014/14/A/ST9/00121. The UCSC transient team is supported in part by NSF grant AST-1518052, NASA/Swift grant 80NSSC19K1386, the Gordon & Betty Moore Foundation, the Heising-Simons Foundation, and by a fellowship from the David and Lucile Packard Foundation to R.J.F.

Some of the observations were obtained using the Southern African Large Telescope (SALT) as part of the Large Science Programme on transients (2016-2-LSP-001; PI: Buckley). Polish participation in SALT is funded by grant no. MNiSW DIR/WK/2016/07.

This paper includes data gathered with the 6.5 m Magellan Telescopes located at Las Campanas Observatory, Chile.

The analysis is based on observations obtained at the international Gemini Observatory, a program of NSF's OIR Lab, which is managed by the Association of Universities for Research in Astronomy (AURA) under a cooperative agreement with the National Science Foundation, on behalf of the Gemini Observatory partnership: the National Science Foundation (United States), National Research Council (Canada), Agencia Nacional de Investigación y Desarrollo (Chile), Ministerio de Ciencia, Tecnología e Innovación (Argentina), Ministério da Ciência, Tecnologia, Inovações e Comunicações (Brazil), and Korea Astronomy and Space Science Institute (Republic of Korea).

This research uses data obtained through the Telescope Access Program (TAP), which has been funded by the National Astronomical Observatories of China, the Chinese Academy of Sciences, and the Special Fund for Astronomy from the Ministry of Finance

This research was partially supported by the Australian Government through the Australian Research Council's Discovery Projects funding scheme (project DP200102471).

Parts of this research were supported by the Australian Research Council Centre of Excellence for All Sky Astrophysics in 3 Dimensions (ASTRO 3D), through project number CE170100013.

This research uses services or data provided by the NOAO Data Lab. NOAO is operated by the Association of Universities for Research in Astronomy (AURA), Inc. under a cooperative agreement with the National Science Foundation.

This research draws upon DECam data as distributed by the Science Data Archive at NOAO. NOAO is operated by the Association of Universities for Research in Astronomy (AURA) under a cooperative agreement with the National Science Foundation.

This project used data obtained with the Dark Energy Camera (DECam), which was constructed by the Dark Energy Survey (DES) collaboration. Funding for the DES Projects has been provided by the U.S. Department of Energy, the U.S. National Science Foundation, the Ministry of Science and Education of Spain, the Science and Technology Facilities Council of the United Kingdom, the Higher Education Funding Council for England, the National Center for Supercomputing Applications at the University of Illinois at Urbana-Champaign, the Kavli Institute of Cosmological Physics at the University of Chicago, Center for Cosmology and AstroParticle Physics at the Ohio State University, the Mitchell Institute for Fundamental Physics and Astronomy at Texas A&M University, Financiadora de Estudos e Projetos, Fundação Carlos Chagas Filho de Amparo, Financiadora de Estudos e Projetos, Fundação Carlos Chagas Filho de Amparo à Pesquisa do Estado do Rio de Janeiro, Conselho Nacional de Desenvolvimento Científico e Tecnológico and the Ministério da Ciência, Tecnologia e Inovação, the Deutsche Forschungsgemeinschaft, and the Collaborating Institutions in the Dark Energy Survey.

The Collaborating Institutions are Argonne National Laboratory, the University of California at Santa Cruz, the University of Cambridge, Centro de Investigaciones Enérgeticas, Medioambientales y Tecnológicas-Madrid, the University of Chicago, University College London, the DES-Brazil Consortium, the University of Edinburgh, the Eidgenossische Technische Hochschule (ETH) Z urich, Fermi National Accelerator Laboratory, the University of Illinois at Urbana-Champaign, the Institut de Ciències de l'Espai (IEEC/CSIC), the Institut de Física d'Altes Energies, Lawrence Berkeley National Laboratory, the Ludwig-Maximilians Universit at Munchen and the associated Excellence Cluster Universe, the University of Michigan, the National Optical Astronomy Observatory, the University of Nottingham, the Ohio State University, the OzDES Membership Consortium, the University of Pennsylvania, the University of Portsmouth, SLAC National Accelerator Laboratory, Stanford University, the University of Sussex, and Texas A&M University.

Based on observations at Cerro Tololo Inter-American Observatory, National Optical Astronomy Observatory (Prop. ID 2018A-0251, PI D. Finkbeiner), which is operated by the Association of Universities for Research in Astronomy (AURA) under a cooperative agreement with the National Science Foundation.

Software: HEAsoft (HEASARC 2014), GALFIT (Peng et al. 2002), PySALT (Crawford et al. 2010, 2016), polSALT (K. Nordsieck & D. Groenewald 2020, in preparation), CASA (McMullin et al. 2007), IRAF (Tody 1986, 1993), ISIS (Alard & Lupton 1998; Alard 2000), FAST (Kriek et al. 2009), MOSFiT (Guillochon et al. 2017).

ORCID iDs

Thomas W.-S. Holoien https://orcid.org/0000-0001-9206-3460
Katie Auchettl https://orcid.org/0000-0002-4449-9152
Michael A. Tucker https://orcid.org/0000-0002-2471-8442
Benjamin J. Shappee https://orcid.org/0000-0003-4631-1149
Shannon G. Patel https://orcid.org/0000-0003-3350-9869
James C. A. Miller-Jones https://orcid.org/0000-0003-3124-2814
Jason T. Hinkle https://orcid.org/0000-0001-9668-2920
Jonathan S. Brown https://orcid.org/0000-0002-1885-6419
Christopher S. Kochanek https://orcid.org/0000-0001-6017-2961
Ping Chen https://orcid.org/0000-0003-0853-6427
Subo Dong https://orcid.org/0000-0002-1027-0990
Jose L. Prieto https://orcid.org/0000-0003-0943-0026
Rachael L. Beaton https://orcid.org/0000-0002-1691-8217
Thomas Connor https://orcid.org/0000-0002-7898-7664
Philip S. Cowperthwaite https://orcid.org/0000-0002-2478-6939
K. Decker French https://orcid.org/0000-0002-4235-7337
Nidia Morrell https://orcid.org/0000-0003-2535-3091
Mariusz Gromadzki https://orcid.org/0000-0002-1650-1518
David A. Coulter https://orcid.org/0000-0003-4263-2228
Georgios Dimitriadis https://orcid.org/0000-0001-9494-179X
Charles D. Kilpatrick https://orcid.org/0000-0002-5740-7747
Anthony L. Piro https://orcid.org/0000-0001-6806-0673
Sjoert van Velzen https://orcid.org/0000-0002-3859-8074

References

Alard, C. 2000, A&AS, 144, 363
Alard, C., & Lupton, R. H. 1998, ApJ, 503, 325
Alexander, K. D., Berger, E., Guillochon, J., Zauderer, B. A., & Williams, P. K. G. 2016, ApJL, 819, L25
Arcavi, I., Gal-Yam, A., Sullivan, M., et al. 2014, ApJ, 793, 38
Auchettl, K., Guillochon, J., & Ramirez-Ruiz, E. 2017, ApJ, 838, 149
Bertin, E., & Arnouts, S. 1996, A&AS, 117, 393
Blagorodnova, N., Gezari, S., Hung, T., et al. 2017, ApJ, 844, 46
Blagorodnova, N., Cenko, S. B., Kulkarni, S. R., et al. 2019, ApJ, 873, 92
Bose, S., Dong, S., Pastorello, A., et al. 2018, ApJ, 853, 57
Breeveld, A. A., Curran, P. A., Hoversten, E. A., et al. 2010, MNRAS, 406, 1687
Brown, J. S., Holoien, T. W.-S., Auchettl, K., et al. 2017, MNRAS, 466, 4904
Brown, J. S., Kochanek, C. S., Holoien, T. W. -S., et al. 2018, MNRAS, 473, 1130
Brown, J. S., Shappee, B. J., Holoien, T. W.-S., et al. 2016, MNRAS, 462, 3993
Brown, T. M., Baliber, N., Bianco, F. B., et al. 2013, PASP, 125, 1031
Bruzual, G., & Charlot, S. 2003, MNRAS, 344, 1000
Buckley, D. A. H., Andreoni, I., Barway, S., et al. 2018, MNRAS, 474, L71
Buckley, D. A. H., Swart, G. P., & Meiring, J. G. 2006, Proc. SPIE, 6267, 62670Z
Burgh, E. B., Nordsieck, K. H., Kobulnicky, H. A., et al. 2003, Proc. SPIE, 4841, 1463
Burrows, D. N., Hill, J. E., Nousek, J. A., et al. 2005, SSR, 120, 165
Cardelli, J. A., Clayton, G. C., & Mathis, J. S. 1989, ApJ, 345, 245
Cenko, S. B., Bloom, J. S., Kulkarni, S. R., et al. 2012, MNRAS, 420, 2684
Chornock, R., Berger, E., Gezari, S., et al. 2014, ApJ, 780, 44
Clemens, J. C., Crain, J. A., & Anderson, R. 2004, Proc. SPIE, 5492, 331
Crawford, S. M., Crause, L., Depagne, É., et al. 2016, Proc. SPIE, 9908, 99082L
Crawford, S. M., Still, M., Schellart, P., et al. 2010, Proc. SPIE, 7737, 773725
Cutri, R. M., Wright, E. L., Conrow, T., et al. 2013, Explanatory Supplement to the AllWISE Data Release Products
Dai, L., McKinney, J. C., Roth, N., Ramirez-Ruiz, E., & Miller, M. C. 2018, ApJL, 859, L20
Dressler, A., Bigelow, B., Hare, T., et al. 2011, PASP, 123, 288
Evans, C. R., & Kochanek, C. S. 1989, ApJL, 346, L13
Gaskell, C. M., & Rojas Lobos, P. A. 2014, MNRAS, 438, L36
Gehrels, N., Chincarini, G., Giommi, P., et al. 2004, ApJ, 611, 1005
Gezari, S., Cenko, S. B., & Arcavi, I. 2017, ApJL, 851, L47
Gezari, S., Chornock, R., Lawrence, A., et al. 2015, ApJL, 815, L5
Gezari, S., Chornock, R., Rest, A., et al. 2012, Natur, 485, 217
Gimeno, G., Roth, K., Chiboucas, K., et al. 2016, Proc. SPIE, 9908, 99082S
Guillochon, J., Nicholl, M., Villar, V. A., et al. 2017, MOSFiT: Modular Open-Source Fitter for Transients, Astrophysics Source Code Library, ascl:1710.006
Guillochon, J., & Ramirez-Ruiz, E. 2013, ApJ, 767, 25
Guillochon, J., & Ramirez-Ruiz, E. 2015, ApJ, 809, 166
Hayasaki, K., Stone, N., & Loeb, A. 2013, MNRAS, 434, 909
Hayasaki, K., Stone, N., & Loeb, A. 2016, MNRAS, 461, 3760
HEASARC, N. 2014, HEAsoft: Unified Release of FTOOLS and XANADU, Astrophysics Source Code Library, ascl:1408.004
Heiles, C. 2000, AJ, 119, 923
Henden, A. A., Levine, S., Terrell, D., & Welch, D. L. 2015, AAS Meeting Abstracts, 225, 336.16
HI4PI Collaboration et al., Ben Bekhti, N., & Flöer, L. 2016, A&A, 594, A116
Hinkle, J. T., Holoien, T. W. S., Shappee, B. J., et al. 2020a, ApJL, 894, 10
Hinkle, J. T., Holoien, T. W.-S., Auchettl, K., et al. 2020b, arXiv:2006.06690
Hoflich, P. 1991, A&A, 246, 481
Holoien, T. W.-S., Brown, J. S., Auchettl, K., et al. 2018, MNRAS, 480, 5689
Holoien, T. W. S., Huber, M. E., Shappee, B. J., et al. 2019b, ApJ, 880, 120
Holoien, T. W.-S., Kochanek, C. S., Prieto, J. L., et al. 2016a, MNRAS, 463, 3813
Holoien, T. W.-S., Kochanek, C. S., Prieto, J. L., et al. 2016b, MNRAS, 455, 2918
Holoien, T. W. S., Vallely, P. J., Auchettl, K., et al. 2019a, ApJ, 883, 111
Holoien, T. W.-S., Prieto, J. L., Bersier, D., et al. 2014, MNRAS, 445, 3263
Hook, I. M., Jørgensen, I., Allington-Smith, J. R., et al. 2004, PASP, 116, 425
Hung, T., Gezari, S., Blagorodnova, N., et al. 2017, ApJ, 842, 29
Kochanek, C. S. 1994, ApJ, 422, 508
Kochanek, C. S. 2016, MNRAS, 461, 371
Kochanek, C. S., Shappee, B. J., Stanek, K. Z., et al. 2017, PASP, 129, 104502
Kriek, M., van Dokkum, P. G., Labbé, I., et al. 2009, ApJ, 700, 221
Krolik, J., Piran, T., Svirski, G., & Cheng, R. M. 2016, ApJ, 827, 127
Lacy, J. H., Townes, C. H., & Hollenbach, D. J. 1982, ApJ, 262, 120
Leloudas, G., Dai, L., Arcavi, I., et al. 2019, ApJ, 887, 218
Lodato, G., & Rossi, E. M. 2011, MNRAS, 410, 359
Lupton, R. 2005, Transformations between SDSS magnitudes and UBVR$_c$I$_c$, http://www.sdss.org/dr5/algorithms/sdssUBVRITransform.html
MacLeod, C. L., Ivezić, Ž., Sesar, B., et al. 2012, ApJ, 753, 106
McConnell, N. J., & Ma, C.-P. 2013, ApJ, 764, 184
McMullin, J. P., Waters, B., Schiebel, D., Young, W., & Golap, K. 2007, in ASP Conf. Ser. 376, Astronomical Data Analysis Software and Systems XVI, ed. R. A. Shaw, F. Hill, & D. J. Bell (San Francisco, CA: ASP), 127
Mockler, B., Guillochon, J., & Ramirez-Ruiz, E. 2019, ApJ, 872, 151
Nordsieck, K. H., Jaehnig, K. P., Burgh, E. B., Kobulnicky, H. A., Percival, J. W., & Smith, M. P. 2003, Proc. SPIE, 4843, 170
Pan, Y.-C., Foley, R. J., Jha, S. W., Rest, A., & Scolnic, D. 2018, ATel, 11865, 1
Patel, S. G., Hong, Y. X., Quadri, R. F., Holden, B. P., & Williams, R. J. 2017, ApJ, 839, 127
Peng, C. Y., Ho, L. C., Impey, C. D., & Rix, H.-W. 2002, AJ, 124, 266
Peterson, B. M., Ferrarese, l., Gilbert, K. M., et al. 2004, ApJ, 613, 682
Phinney, E. S. 1989, Natur, 340, 595
Piran, T., Svirski, G., Krolik, J., Cheng, R. M., & Shiokawa, H. 2015, ApJ, 806, 164
Poole, T. S., Breeveld, A. A., Page, M. J., et al. 2008, MNRAS, 383, 627
Rees, M. J. 1988, Natur, 333, 523
Roming, P. W. A., Kennedy, T. E., Mason, K. O., et al. 2005, SSR, 120, 95
Roth, N., & Kasen, D. 2018, ApJ, 855, 54
Roth, N., Kasen, D., Guillochon, J., & Ramirez-Ruiz, E. 2016, ApJ, 827, 3
Schlafly, E. F., & Finkbeiner, D. P. 2011, ApJ, 737, 103
Serkowski, K., Mathewson, D. S., & Ford, V. L. 1975, ApJ, 196, 261
Shappee, B. J., Prieto, J. L., Grupe, D., et al. 2014, ApJ, 788, 48
Shiokawa, H., Krolik, J. H., Cheng, R. M., Piran, T., & Noble, S. C. 2015, ApJ, 804, 85
Strubbe, L. E., & Murray, N. 2015, MNRAS, 454, 2321
Strubbe, L. E., & Quataert, E. 2009, MNRAS, 400, 2070
Tody, D. 1986, Proc. SPIE, 627, 733

Tody, D. 1993, in ASP Conf. Ser. 52, Astronomical Data Analysis Software and Systems II, ed. R. J. Hanisch, R. J. V. Brissenden, & J. Barnes (San Francisco, CA: ASP), 173
van Velzen, S., Anderson, G. E., Stone, N. C., et al. 2016, Sci, 351, 62
van Velzen, S., Farrar, G. R., Gezari, S., et al. 2011, ApJ, 741, 73
van Velzen, S., Gezari, S., Cenko, S. B., et al. 2019, ApJ, 872, 198
van Velzen, S., Gezari, S., Hammerstein, E., et al. 2020, arXiv:2001.01409
Vinkó, J., Yuan, F., Quimby, R. M., et al. 2015, ApJ, 798, 12
Wevers, T., Pasham, D. R., van Velzen, S., et al. 2019, MNRAS, 488, 4816
Wevers, T., van Velzen, S., Jonker, P. G., et al. 2017, MNRAS, 471, 1694
Wilson, W. E., Ferris, R. H., Axtens, P., et al. 2011, MNRAS, 416, 832
Woudt, P. A., Kraan-Korteweg, R. C., Lucey, J., Fairall, A. P., & Moore, S. A. W. 2008, MNRAS, 383, 445
Wright, E. L., Eisenhardt, P. R. M., Mainzer, A. K., et al. 2010, AJ, 140, 1868